

# Numerical detection of patterns in CPGs: gait patterns in insect movement

R. Barrio<sup>a</sup>, Á. Lozano<sup>b</sup>, M. Rodríguez<sup>c</sup>, S. Serrano<sup>a</sup>

<sup>a</sup>*IUMA, CoDy and Dpto. Matemática Aplicada. Universidad de Zaragoza, E-50009 Zaragoza, Spain*

<sup>b</sup>*IUMA. Centro Universitario de la Defensa, Academia General Militar, Universidad de Zaragoza, E-50090 Zaragoza, Spain*

<sup>c</sup>*CoDy group. Matemática Aplicada. Universidad de Zaragoza, E-50009 Zaragoza, Spain*

---

## Abstract

The study of the synchronization patterns of small neuron networks that control different biological processes has become a growing discipline. This paper is focused on numerical techniques to detect patterns in Central Pattern Generators (CPGs). We develop two techniques that can be used directly in general CPG models: a *lateral phase lag analysis* based on a graphic representation of some Poincaré maps, and a *quasi-Monte Carlo sweeping* with an optimized classification of the different patterns.

As test example we consider a CPG of insect movement consisting of six coupled neurons following the model developed by Ghigliazza and Holmes (2004) for motoneurons in cockroaches. Previous studies in literature analyzed reduced models of dimension two obtained using phase resetting curves and averaging theory. This approach introduces a lot of simplifications that do not cover numerous non-symmetric patterns. We present an analysis of the complete model developed by combining the two proposed techniques, showing symmetric and non-symmetric patterns coexisting for different parameter values, and how the dominant patterns evolve to the tripod movement.

*Keywords:* insect movement gaits, CPGs, neuronal networks, bifurcations

*PACS:* 87.19.lj, 87.19.lm, 05.45.-a

*2000 MSC:* 37Mxx, 37G35

---

## 1. Introduction

Last few years the study of small networks of oscillators and neurons has been an active research subject due to the very large number of applications in several fields [1, 2, 3, 4, 5, 6, 7, 8, 9].

The production of coordinated and rhythmic behaviors in organisms, such as chewing, respiration, walking, crawling and swimming, is a fundamental question in the study of motor control and neuroscience. Many of these behaviors are driven by Central Pattern Generators (CPGs), which are groups of neurons (small biological neuron networks) whose interactions can output rhythmic patterns [10, 11, 12, 13] resembling normal “rhythmic motor pattern production” (like in locomotive patterns [14, 15, 16] or in the direct-reverse flow of the circulatory system in leeches [17, 18]) even in isolation from motor and sensory feedback from limbs and other muscle targets. Although anatomical details of CPGs are only known in few cases, they have been shown to originate from the spinal cord of various vertebrates and to depend on relatively small and autonomous neuron networks. The classical view of

---

*Email addresses:* rbarrio@unizar.es (R. Barrio), alozano@unizar.es (Á. Lozano), marcos@imark.es (M. Rodríguez), sserrano@unizar.es (S. Serrano)

13 CPGs, as specific networks of neurons dedicated to this function alone, has been supported by numerous  
 14 experiments with invertebrates. In these cases, it is possible to identify many of the key neuronal elements  
 15 (mostly interneurons) composing a CPG, leading to an easier analysis. Besides, it is possible to record  
 16 and to biophysically analyze these neurons and their synaptic interactions. There is a growing interest  
 17 in the analysis of basic CPG structures for different animal motion [19], like biped [20], quadruped [6]  
 18 and hexapod motion [21]. In the case of insect movement, the basic CPGs models use a set of six con-  
 19 nected motoneurons [21, 22, 23, 24], but more complex models have been developed that also take into  
 20 account the biomechanics of the legs [25, 26, 27]. Moreover, these studies have applications in robotics  
 21 [28, 29, 30, 31].

22 Different animals have different gaits in their locomotion characterized by the number of legs they  
 23 use. In the case of insects, hexapods, the basic observed movement patterns are slow metachronal gait,  
 24 where the hind, middle and front legs on one side swing in succession followed by those on the other side  
 25 (one leg is in swing at any time), tetrapod gait (four legs on the ground every time) and tripod gait (three  
 26 legs on the floor). The use of one or another gait is mainly due to the locomotion speed of the animal  
 27 [22]. Figure 1 illustrates tetrapod and tripod theoretical patterns [21], and experimental data analysis  
 28 for the tripod case (taken from Figure 1 of [23]).

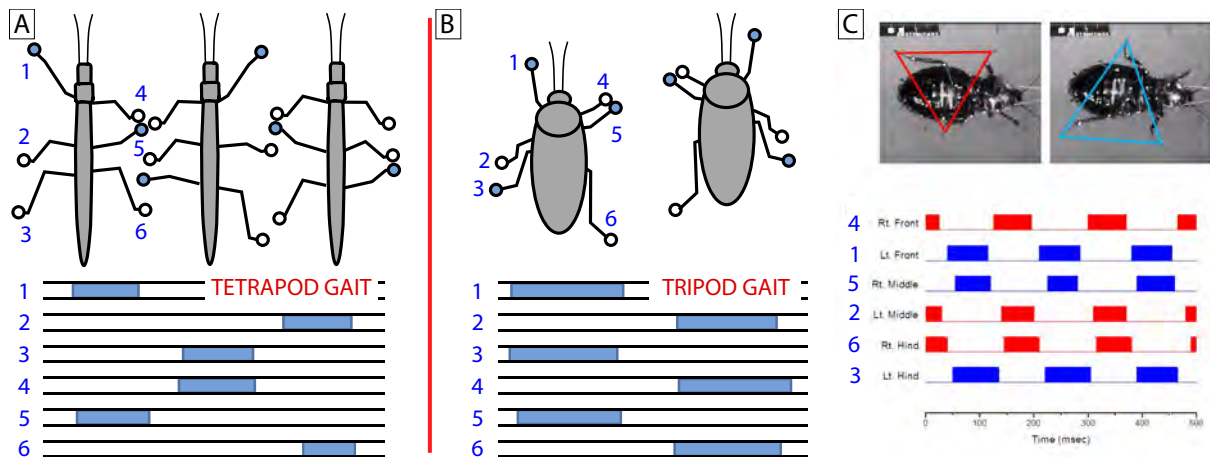


Figure 1: Panels A and B illustrate the schematic tetrapod and tripod movement gaits [21], and boxes indicate times when each leg is in swing. Panel C (taken from Figure 1 of [23]) shows experimentally the tripod gait pattern for a cockroach on a tether.

29 In this paper we propose numerical techniques to detect patterns in CPGs, focusing on locating gait  
 30 patterns in insect locomotion. The two proposed techniques are applied to a particular CPG model but  
 31 it can be used as well in generic small networks. In the description of the numerical methods we provide  
 32 some comments on possible generalizations. The test example is a CPG with six coupled neurons, where  
 33 each neuron follows the model of Ghigliazza and Holmes [24] for motoneurons in cockroaches. Note that  
 34 this model develops a bursting behavior for the interesting parametric region [24], but in literature, for  
 35 other insects, models that do not generate a bursting regime are used [32]. Since this model is four  
 36 dimensional for connected neurons, the complete CPG model is a 24-dimensional ODE system. We  
 37 use an inhibitory nearest neighbor coupling. In order to analyze insect locomotion, several simplification  
 38 approaches are commonly used. For instance, in [30, 33] a basic CPG consisting of 6 oscillators was studied  
 39 using symmetries and algebraic techniques. More recently, several studies in literature [24, 32, 34] focus  
 40 on the analysis of reduced two dimensional models obtained using infinitesimal Phase Resetting Curves  
 41 (iPRC) [35, 36] and averaging theory. These small reduced models allow several analytical studies. The

42 main limitations of these approaches are that they introduce simplifications that do not cover numerous  
43 non-symmetric patterns, shown, for example, in [37], and it is difficult to introduce complicated models.  
44 Therefore, the aim of this paper is to develop techniques to study the complete CPG without any  
45 simplification. For that purpose, a previous study of the dynamics of an isolated neuron allows us to  
46 develop a “roadmap” that guides the changes in the different gaits. Later, we present two techniques that  
47 can be used directly in the complete model. The first one (an extension of the technique introduced in  
48 [51] for 3-cell CPGs), lateral phase lag analysis, is based on a graphic representation of Poincaré maps for  
49 suitable 2D sets of initial conditions. The second one, a quasi-Monte Carlo sweeping, uses an optimized  
50 classification of the different patterns of the complete problem. The combined use of both techniques  
51 shows symmetric and non-symmetric patterns that coexist for different parameter values and how the  
52 dominant patterns evolve towards the tripod movement. In addition, the techniques introduced in this  
53 document also allow to study heterogeneous CPGs in future works, and also to consider other CPGs.  
54 Recently, a small heterogeneity has been considered in [38, 39], where it is shown that the introduction  
55 of heterogeneities eliminates several patterns in CPGs.

56 This paper is organized as follows. In Section 2, we introduce the ion-channel model for bursting  
57 motoneurons in cockroaches developed in [24] and we study the different parametric behaviors and bifur-  
58 cations. In Section 3, we describe the insect movement CPG, and different reductions used in references  
59 [24, 32, 34]. In Section 4, we introduce a technique based on the phase lag analysis of the two sides of the  
60 insect and on the coupled middle legs. The potential of this technique is illustrated on the test problem.  
61 In Section 5, we describe a technique based on a quasi-Monte Carlo method to study the complete model  
62 in order to detect non-symmetric patterns as well. With this technique we develop a transition panel  
63 that shows the dominant patterns along a selected parametric line (which represents a generic situation).  
64 Finally, some conclusions are presented.

## 65 2. Isolated neuron dynamics

66 In this paper, we consider as test example the mathematical neuron burster of Ghigliazza and  
67 Holmes [24]. It models the neurons of the local network driving the movement of a cockroach. This  
68 model takes into account a fast nonlinear calcium current,  $I_{Ca}$ , a slower potassium current  $I_K$ , an ad-  
69 ditional very slow current  $I_{KS}$ , a linear leakage current  $I_L$  and an external current  $I_{ext}$ . The system is  
70 described by an ODE system of dimension three:

$$\begin{cases} C\dot{v} &= -[I_{Ca} + I_K + I_L + I_{KS}] + I_{ext}, \\ \dot{m} &= \frac{\epsilon}{\tau_m(v)} [m_\infty(v) - m], \\ \dot{w} &= \frac{\delta}{\tau_w(v)} [w_\infty(v) - w], \end{cases} \quad (1)$$

with the auxiliary ionic current functions defined by

$$\begin{aligned} I_{Ca} &= g_{Ca} n_\infty(v) (v - E_{Ca}), & I_K &= g_K m (v - E_K), \\ I_L &= g_L (v - E_L), & I_{KS} &= g_{KS} w (v - E_K) \end{aligned}$$

and where the different time scales and steady state gating variables are

$$\begin{aligned} \tau_m(v) &= \operatorname{sech}(k_{0_K} (v - v_K^{th})/2), & \tau_w(v) &= \operatorname{sech}(k_{0_{KS}} (v - v_{KS}^{th})/2), \\ m_\infty(v) &= (1 + e^{-2k_{0_K} (v - v_K^{th})})^{-1}, & w_\infty(v) &= (1 + e^{-2k_{0_{KS}} (v - v_{KS}^{th})})^{-1}, \\ n_\infty(v) &= (1 + e^{-2k_{0_{Ca}} (v - v_{Ca}^{th})})^{-1}. \end{aligned}$$

71 In Section 3, we will add an extra variable  $s(t)$  to take into account the synopsis of the CPG. In our  
72 analysis, we will fix all the parameters except  $I_{ext}$  and  $v_{KS}^{th}$ , which we will leave free as bifurcation

73 parameters. Other parameters depend mainly on the kind of insect. We use along the paper the values  
 74 of the fixed parameters taken from [24]:

$$\begin{aligned}
 C &= 1.2, & E_{Ca} &= 120.0, & E_K &= -80.0, & E_L &= -60.0, & \delta &= 0.005, \\
 \epsilon &= 4.9, & g_{Ca} &= 4.4, & g_K &= 8.0, & g_{KS} &= 0.15, & g_L &= 2.0, \\
 k_{0Ca} &= 0.055, & k_{0K} &= 0.1, & k_{0KS} &= 0.4, & v_{Ca}^{th} &= -1.2, & v_K^{th} &= 2.0.
 \end{aligned}
 \tag{2}$$

75 We begin to study the model (1) of an isolated neuron because it will give us a “roadmap” to know  
 76 where to analyze the complete model of the CPG. Moreover, it provides dynamical information used to  
 77 calibrate the numerical tools of the next sections. To find out which region to start studying, we use  
 78 numerical techniques for detection and continuation of bifurcations (the software AUTO [40]).

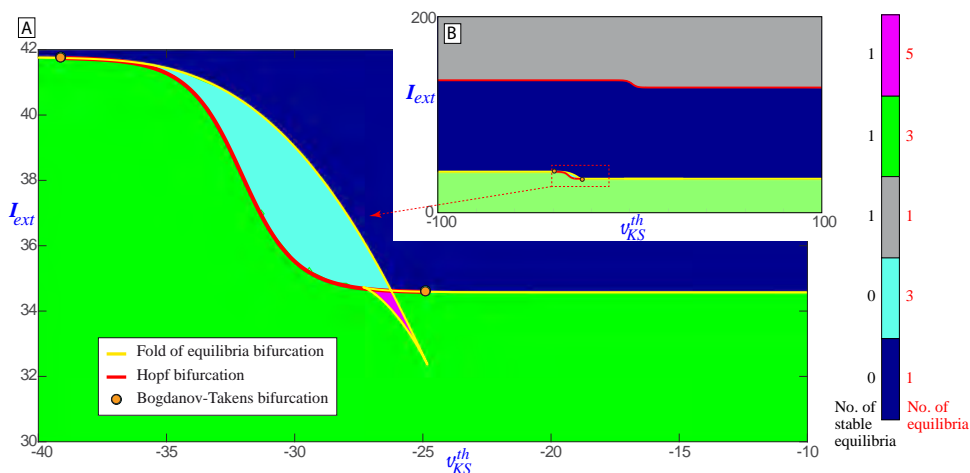


Figure 2: Different regions of the biparametric space based on the number of equilibria and their stability. Such regions are bounded by bifurcation curves in which some equilibrium point changes its stability (Hopf) or collides with another one and disappear (fold). In the upper right corner picture (plot (B)) a larger region of the parametric space is shown, and it can be observed how a new Hopf bifurcation curve appears for large values of the parameter  $I_{ext}$ .

79 Figure 2 presents a biparametric plot showing together the number of equilibria, their stability and  
 80 several bifurcation lines. Note how the curves for Hopf and fold bifurcations of equilibria delimit regions  
 81 with different number of equilibria or with different stability. There is a stable equilibrium point in the  
 82 green, orange and gray regions, while in the others all are unstable. On the other hand, we can see that  
 83 there is a region (marked in cyan) around which there are different changes in the number and type of  
 84 equilibria. This region and the adjacent one in blue are the areas in which all equilibria are unstable. This  
 85 fact explains why the bursting and spiking regions are in the cyan and blue areas. These areas constitute  
 86 the most interesting region for us, since bursting behavior is the dynamic considered for cockroaches in  
 87 [24, 34]. Therefore, we will study this region in detail. The upper right plot presents a larger region of  
 88 the parametric space to show that, for larger values of the external current  $I_{ext}$ , a new Hopf bifurcation  
 89 curve appears (note that most of the fold/hom burster models have two Hopf bifurcations).

90 Figure 3 shows the slow-fast decomposition (first developed in [41]) of the model (1) taking the small  
 91 parameter  $\delta = 0$ ,  $v_{KS}^{th} = -25$  and for two values of  $I_{ext}$  ( $I_{ext} = 35.5$  and  $100$ ), located in the bursting  
 92 and spiking regions, respectively. The spiking (or fast) manifold,  $\mathcal{M}_{fast}$  (formed by stable limit cycles of  
 93 the limit case), is shown in blue; the slow manifold,  $\mathcal{M}_{slow}$  (formed by the equilibria of the limit case),  
 94 is shown in green. The stable periodic orbit of the complete model is shown in red, and we can observe  
 95 the well-known phenomenon, explained by singular perturbation theory and Fenichel’s theorems, that

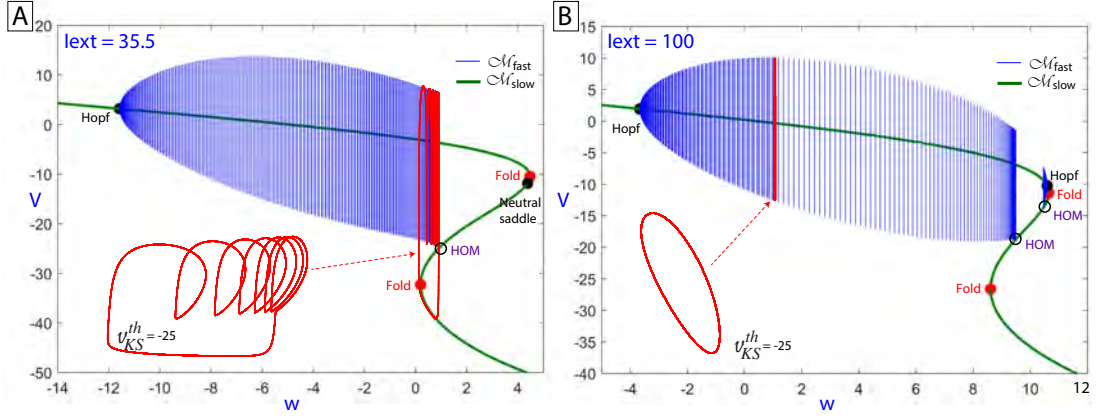


Figure 3: Classical slow-fast decomposition of model (1) illustrating the slow manifold of equilibria ( $\mathcal{M}_{slow}$ ) and the fast (spiking) manifold ( $\mathcal{M}_{fast}$ ) of limit cycles of the fast subsystem of the neuron model. Fo1d stands for fold (or saddle-node) bifurcations of equilibria, Hopf denotes the Hopf bifurcation points and HOM the homoclinic bifurcation points.

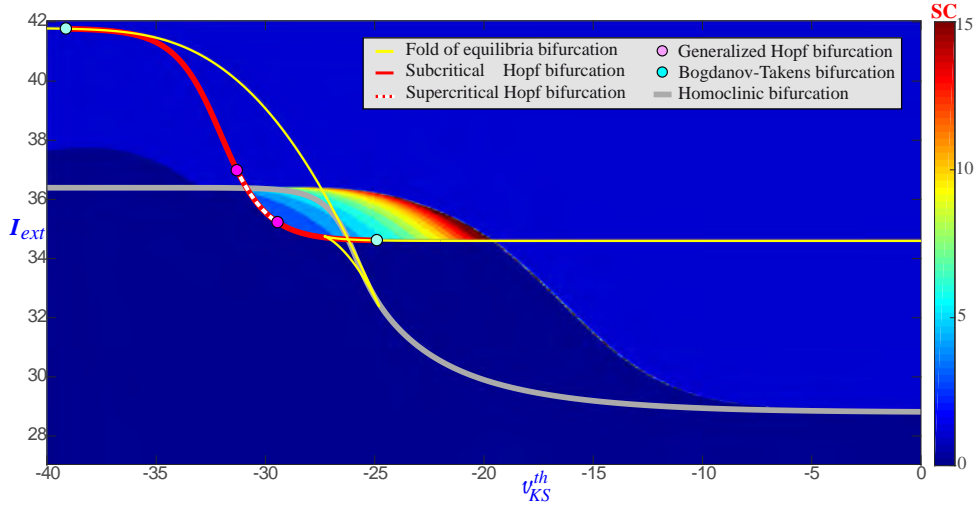


Figure 4: Different bifurcation curves and bifurcation points of codimension two superimposed on the spike-counting plate. Different colors mark different number of spikes in the attracting orbit (up to 15 spikes). We can see how some parts of different bifurcation curves delimit the region of bursting.

96 the orbit (for small enough parameter  $\delta$ ) follows both manifolds on some parts of its trajectory. On the  
 97 first case,  $I_{ext} = 35.5$ , the orbit is a classical bursting orbit of fold/homoclinic type [42] because the  
 98 termination of the fast subregime is due to the existence of a homoclinic bifurcation in the phase space of  
 99 the fast subsystem. This point is marked in the Figure 3. Note that, for this value of the external current,  
 100 there is just one supercritical Hopf bifurcation on the upper depolarized branch of  $\mathcal{M}_{fast}$ . If  $I_{ext}$  grows,  
 101 the neutral-saddle point crosses the fold bifurcation becoming another supercritical Hopf bifurcation, as  
 102 the picture for  $I_{ext} = 100$  shows. Now the orbit presents a depolarized spiking state rotating around the  
 103 spiking manifold.

104 In the following, since we are only interested in the fold/hom bursting region, we will focus on that  
 105 part of the parametric phase space. That is why, in Figure 4, we represent in the area of interest, along

106 with some bifurcation curves, the number of spikes of the limit cycle of the system on each point of the  
 107 biparametric plane when starting from fixed initial conditions. This figure shows how some parts of the  
 108 bifurcation curves delimit the fold/hom bursting region. Other bifurcation curves, in particular a curve of  
 109 homoclinic bifurcations, are represented, as well as some codimension two bifurcation points. Note that  
 110 recently several codimension two homoclinic bifurcation points have been linked with the spike-adding  
 111 process [43, 44].

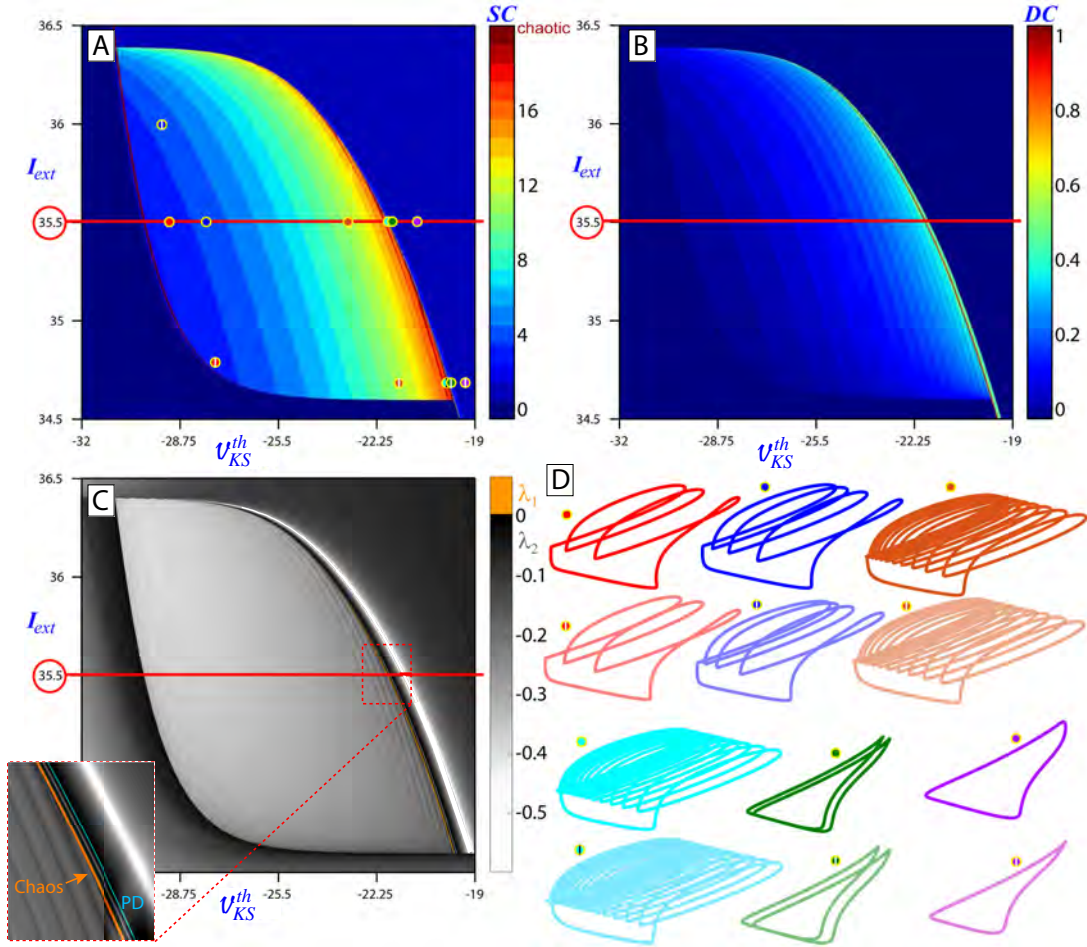


Figure 5: Analysis of the bursting region using different techniques: (A) spike-counting, (B) duty cycle and (C) Lyapunov exponents ( $\lambda_1$  and  $\lambda_2$ ). All of them provide similar information but with a different point of view. Small zoom on plot (C) shows the narrow chaotic band and a period-doubling (PD) bifurcation curve. In plot (D) different stable periodic orbits are represented. These orbits are attractors for the pointed values of parameters in the figure of the spike-counting (A), by the circle of the corresponding color. Some of the limit cycles show a period-doubling bifurcation that finally leads to chaotic behavior.

112 From previous studies in literature, it has been shown that the main characteristics of the model, that  
 113 is, the bursting frequency, spiking frequency and the duty cycle can be easily modulated by changing  
 114 most of the parameters. We have observed that we can use  $I_{ext}$  or  $v_{KS}^{th}$  as our main parameters in our  
 115 neuron model. Note, as indicated in [24], that the bursting frequency and duty cycle of CPG interneurons  
 116 are the main responsible for speed adjustment, while spiking frequencies are involved in force production.

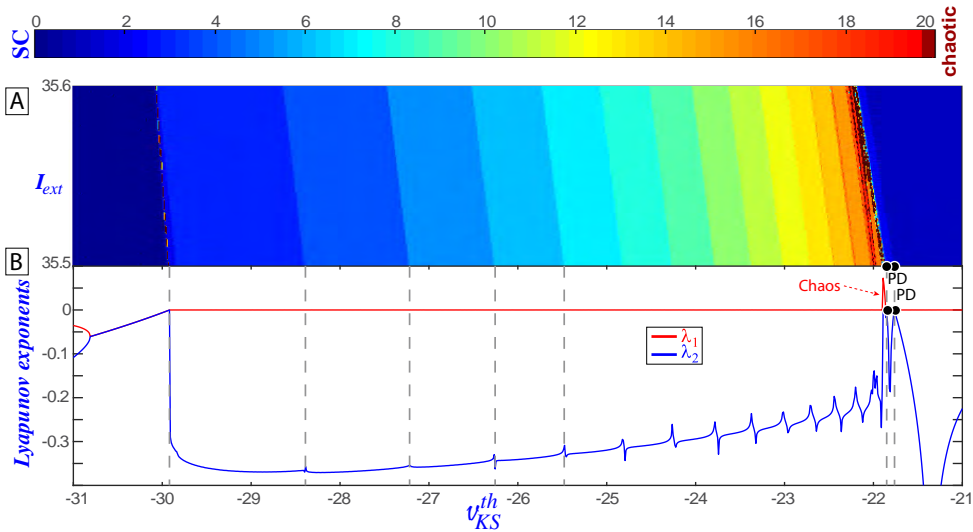


Figure 6: Analysis of the line  $I_{ext} = 35.5$  on the region of bursting using different techniques: (A) spike-counting in a band around this value and (B) the first two Lyapunov exponents ( $\lambda_1$  and  $\lambda_2$ ). The small chaotic interval is pointed as well as two period-doubling (PD) bifurcation points.

117 Therefore, we will focus on the changes of bursting frequency and duty cycle since our aim is to study  
 118 the different gait patterns.

119 Once we have fixed our parametric plane ( $v_{KS}^{th}$ ,  $I_{ext}$ ) and the region of the “roadmap” that we want  
 120 to study, we use different techniques to analyze the dynamics existing there. Thus, Figure 5 shows the  
 121 results obtained with different brute force techniques: in the upper left corner (A), the spike-counting  
 122 technique; in the upper right corner (B) the value of the duty cycle (quotient between the time in which  
 123 the neuron is active and the period of the orbit, so this value will always be between 0 and 1); in the lower  
 124 left corner (C) the first (in the chaotic region) and the second (in the regular region) Lyapunov exponents  
 125 ( $\lambda_1$  and  $\lambda_2$ , respectively). Note that there is a narrow band of chaotic behavior (orange color) close to  
 126 the edge of the bursting region, and curves of period-doubling bifurcations in the spiking area (see the  
 127 zoom on the bottom-left part of plot (C)). The color circles that appear in the picture corresponding to  
 128 the spike-counting technique, plot (A), indicate the values of the parameters for the orbits shown in (D),  
 129 which are the attractors of the system. If we move along the horizontal line, from left to right, we observe  
 130 an increase in the number of spikes due to the spike-adding process (and, if we see the corresponding  
 131 duty cycle picture, an increase in its value). For the region with depolarized spiking state (on the right  
 132 part) we present four orbits showing a period-doubling bifurcation. We can see that the three techniques  
 133 mark bands in the bursting region corresponding to bursters with the same number of spikes. The plotted  
 134 orbits show that the behavior within each strip is qualitatively identical, being different from one band  
 135 to another.

136 Note that although the global image in Figure 5 provided by the three sweeping techniques is similar,  
 137 each one has its own peculiarities. For example, the spike-counting technique unambiguously marks each  
 138 of the bands. The other two techniques mark the edges of the bands, but it is difficult to distinguish  
 139 one band from another. On the contrary, although the duty cycle increases with the number of spikes,  
 140 points with the same number of spikes appear with different duty cycle values. The Lyapunov exponents  
 141 detect both the spike-adding and period-doubling (the reason is that in the spike-adding process fold  
 142 and period-doubling bifurcations of periodic orbits are involved) and the existence of chaos. However,  
 143 its value is not unique along a strip, nor necessarily different between different bands. Figure 6 shows

144 an analysis of the line  $I_{ext} = 35.5$  for the bursting region. This study points the existence of a narrow  
 145 chaotic region close to  $v_{KS}^{th} = -22$ , at the limit between bursting and spiking behavior (Terman [45]  
 146 studied this chaotic behavior in the change from spiking to bursting). Moreover, we can observe a chain  
 147 of period-doubling bifurcations leading to this chaotic region. In the plots of Figure 5(D) there are some  
 148 examples of the limit cycles before and after the first period-doubling bifurcation, and on Figure 6 the  
 149 Lyapunov exponents curve also marks this bifurcation (note that for the period-doubling bifurcation the  
 150 second Lyapunov exponent reaches the value 0 and goes down [46, 47]).

### 151 3. Insect movement CPG: complete model and reductions

After studying in some detail the dynamics of one isolated motoneuron, we study now a CPG (we  
 follow the formalism of [24]) modelling the insect movement: a network of six mutually inhibiting iden-  
 tical neurons (see the left picture of Figure 7). The inhibitory coupling can be achieved via synapses  
 that produce negative postsynaptic currents, or presynaptically by depressing a synapse. In our case  
 we consider negative postsynaptic currents generated via the additional term,  $(I_{syn})_i$ , in the potential  
 differential equation for each neuron

$$C\dot{v}_i = -[(I_{Ca})_i + (I_K)_i + (I_L)_i + (I_{KS})_i] + I_{ext} - (I_{syn})_i.$$

152 The current  $-(I_{syn})_i$  can be positive (depolarizing) giving excitatory synapses, or negative (hyperpolariz-  
 153 ing) giving inhibitory synapses. The different values of the extra current  $(I_{syn})_i$  for each neuron potential  
 154  $v_i$  are:

$$\begin{aligned} (I_{syn})_1 &= c_1 g_{syn} s_4 (v_1 - E_s^{post}) + c_5 g_{syn} s_2 (v_1 - E_s^{post}), \\ (I_{syn})_2 &= c_2 g_{syn} s_5 (v_2 - E_s^{post}) + c_4 g_{syn} s_1 (v_2 - E_s^{post}) + c_7 g_{syn} s_3 (v_2 - E_s^{post}), \\ (I_{syn})_3 &= c_3 g_{syn} s_6 (v_3 - E_s^{post}) + c_6 g_{syn} s_2 (v_3 - E_s^{post}), \\ (I_{syn})_4 &= c_1 g_{syn} s_1 (v_4 - E_s^{post}) + c_5 g_{syn} s_5 (v_4 - E_s^{post}), \\ (I_{syn})_5 &= c_2 g_{syn} s_2 (v_5 - E_s^{post}) + c_4 g_{syn} s_4 (v_5 - E_s^{post}) + c_7 g_{syn} s_6 (v_5 - E_s^{post}), \\ (I_{syn})_6 &= c_3 g_{syn} s_3 (v_6 - E_s^{post}) + c_6 g_{syn} s_5 (v_6 - E_s^{post}), \end{aligned}$$

using the additional synapse variables  $s_i$  defined by the differential equation

$$\dot{s}_i = \alpha s_\infty(v_i)(1 - s_i) - \beta s_i,$$

where

$$s_\infty(v) = \frac{T_{max}}{1 + e^{-k_s(v - E_s^{pre})}}.$$

155 The parameter  $g_{syn}$  denotes the synaptic strength, and we have considered a voltage based synapse model  
 156 as in [24, 32, 34].

Along all the paper we have used the same parameter values as in [24]:

$$g_{syn} = 0.015, \quad E_s^{pre} = 2.0, \quad E_s^{post} = -70.0, \quad T_{max} = 0.002, \quad \alpha = 5000.0, \quad \beta = 0.18, \quad k_s = 0.22.$$

157 In the selection of the network parameters  $\{c_i\}$ , we assume contralateral symmetry (between left and  
 158 right side) and the balance conditions

$$c_1 + c_5 = c_2 + c_4 + c_7 = c_3 + c_6,$$

159 and

$$c_4 = c_7, \quad c_5 = c_6, \quad c_1 = c_3.$$

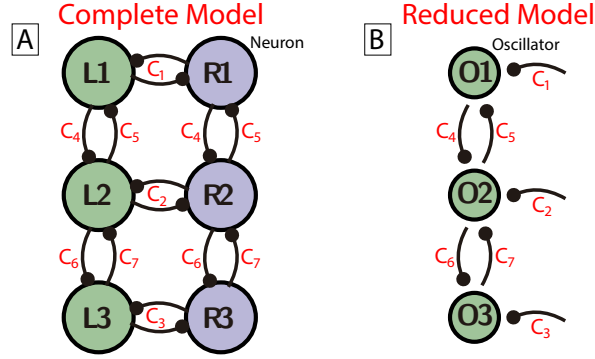


Figure 7: Complete CPG model and reduced phase differences model.

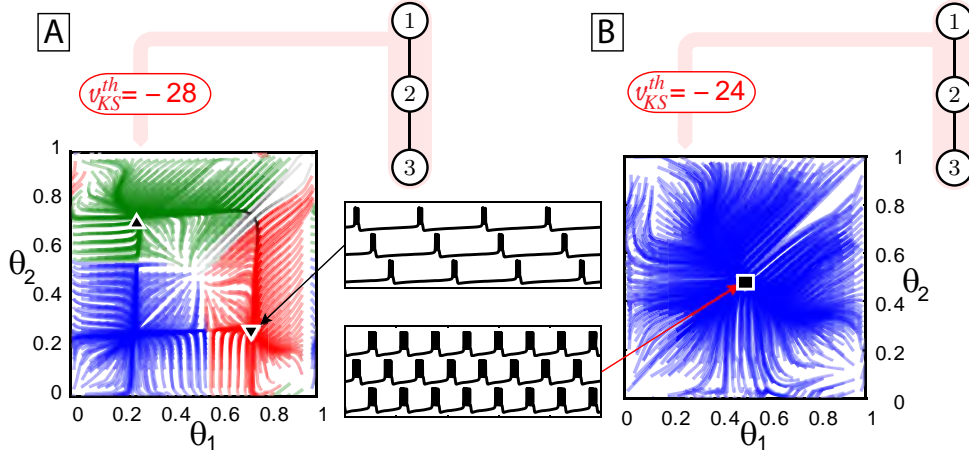


Figure 8: Phase space evolution showing phase differences of the reduced model for the values  $v_{KS}^{th} = -28$  and  $-24$  in the line  $I_{ext} = 35.5$ . Left phases diagram (A) contains two attracting points (triangles) corresponding with tetrapod gait (in addition to the equilibrium point represented in blue); while plot (B) shows a single attracting point in blue corresponding with tripod gait. Note that both blue patterns satisfy  $\theta_1 = \theta_2$ , but with different delay with respect to the middle leg.

160 So, by symmetry, we do not differentiate forward and backward movements in our tests. On the other  
 161 hand, we have set their values as

$$c_4 = c_7 = \frac{1}{2}, \quad c_1 = c_2 = c_3 = c_5 = c_6 = 1.$$

162 In order to simplify the study of the insect movement CPG, different approaches have been adopted  
 163 in the literature, such as the use of symmetries to obtain the basic patterns of the CPG [30, 33]. More  
 164 recently, several studies [24, 32, 34] use infinitesimal Phase Resetting Curves (iPRC) [35, 36] and averaging  
 165 theory to analyze reduced models of the complete CPG. It allows us to perform several analytical studies,  
 166 to detect most of the main patterns in the system, and to study the transitions between them. Using  
 167 iPRC, they reduce the problem of dimension 24 to 6 oscillators and, later, using symmetries, to just 3  
 168 oscillators with phases  $\phi_i$  (and therefore only 2 equations for the phase differences,  $\theta_1 = \phi_1 - \phi_2$  and

169  $\theta_2 = \phi_3 - \phi_2$ , and so the problem is reduced to the dynamics in a torus):

$$\begin{cases} \dot{\theta}_1 = (c_1 - c_2)H\left(\frac{2}{3} - \eta; \xi\right) + c_5H(-\theta_1; \xi) - c_4H(\theta_1; \xi) - c_7H(\theta_2; \xi), \\ \dot{\theta}_2 = (c_3 - c_2)H\left(\frac{2}{3} - \eta; \xi\right) + c_6H(-\theta_2; \xi) - c_4H(\theta_1; \xi) - c_7H(\theta_2; \xi). \end{cases}$$

170 For details of these reductions and the coupling function  $H$  see [34]. In this case, moving in the line  
 171 defined by  $I_{ext} = 35.5$  in the parametric plane of Figure 5 we obtain, with the above phase differences  
 172 model, the results of Figure 8. This figure shows that, increasing the value of  $v_{KS}^{th}$ , the reduced model has  
 173 different gait patterns (associated with the attracting points on the phase diagrams). Note that the time  
 174 evolution of the voltages shows that at the points marked with a triangle on plot (A), and considering  
 175 the complete network and the symmetries used to reduce the system, we have a tetrapod movement with  
 176 two legs moving at the same time. The point marked with a square on plot (B) will develop a tripod  
 177 movement with three legs moving simultaneously. Similar results can be observed in Figures 10, 13 and  
 178 14 of [34] with different values of  $\delta$  and  $I_{ext}$ . The main limitation of this approach is that it introduces  
 179 a lot of simplifications that do not cover numerous non-symmetric patterns. Therefore, the main goal  
 180 of this paper is to develop numerical techniques to study the complete network without simplifications.  
 181 This will allow, in subsequent works, to perform studies breaking any symmetry or homogeneity in the  
 182 complete CPG, or to study different CPGs.

#### 183 4. Lateral phase lag analysis: basic patterns

184 To obtain an analysis similar to the one developed in [34] but for the complete model, we have  
 185 to overcome two difficulties. First of all, we want to work with the original neuron model, without  
 186 approaching it by an oscillator. Secondly, we are going to work with the model of six neurons, so that we  
 187 can later analyze models of the CPG eliminating symmetries or with different neurons within the CPG.  
 188 To solve the first point, we follow the techniques described in [5] to study a CPG of three neurons. For  
 189 the second point, we can decompose the CPG dynamics of 6 neurons into two blocks, the left and the  
 190 right side of the animal.

##### 191 4.1. Numerical method: lateral phase lag analysis

192 In the case of having oscillators, one may obtain directly the equations of the delays of the different  
 193 oscillators with respect to a leading one, providing an easy representation in terms of the phase space  
 194 directly (as commented briefly in the previous section using the iPRC approach for small CPGs). When  
 195 using neurons, detailed studies of rhythms generated by neuronal circuits show that they can be reduced  
 196 to the analysis of fixed points (FPs) and invariant circles (ICs) of Poincaré return maps for phase lags  
 197 between constituent bursters [5].

198 The case of 3-neuron CPGs has been studied in detail in [4, 5] and their approach is the following  
 199 (we include it for completeness): by choosing the second neuron (in our case) as the reference one, we  
 200 introduce the absolute phase lags  $\{\phi_{12}^{(n)}, \phi_{32}^{(n)}\}$ , as shown in Figure 9(A). Note that the main difference of  
 201 this approach to the one of the network of oscillators of Figure 8 is that now we do not plot the phase  
 202 space but a set of discrete points (giving a polygonal line once connected) corresponding to the Poincaré  
 203 return map at a selected value of the voltage variable. Once obtained the phase lags, we normalize them,  
 204  $d_{12}^{(n)} = \phi_{12}^{(n)}/P(n)$  and  $d_{32}^{(n)} = \phi_{32}^{(n)}/P(n)$ , with  $P(n)$  the period or recurrent time of the reference burster  
 205 on the  $n$ -bursting cycle, giving the relative phase lags. The resulting curves, using enough initial phase  
 206 lags, give us the desired 2D return map showing time evolutions of phase lags transitioning toward stable  
 207 FPs corresponding to phase-locked rhythms (the patterns) produced by the network under consideration.  
 208 Left plot of Figure 9(C) shows the relative phase lags corresponding to the three neurons of the left side  
 209 of the insect, studying in this case the delays with respect to the middle-leg neuron (neuron 2). The

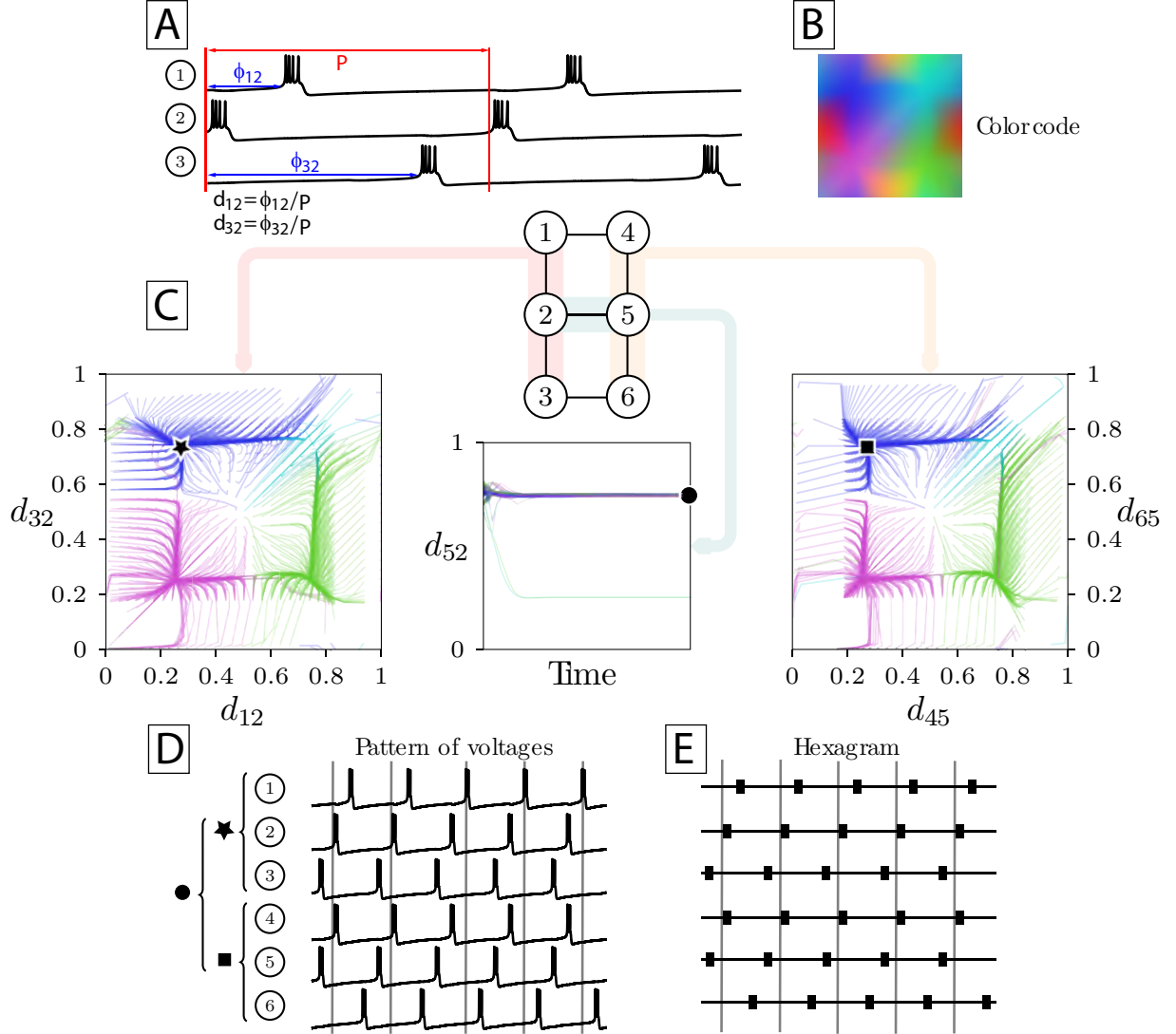


Figure 9: (A): 3-cell network (left side of the CPG) voltage waveforms with one recurrent time  $P$  and absolute phase lags  $\phi_{12}, \phi_{32}$  relative to the reference burster 2 at a selected value of the voltage variable for this recurrent time. (B) Color code identifying the 2D area of the convergence of the 2D return map generated by the Poincaré map. (C) Lateral phase lag analysis of the complete model of CPG with 6 neurons ( $I_{ext} = 35.5$  and  $v_{KS}^{th} = -28$ ). This representation is composed by three pictures: two lateral phase lags transitions and one central picture with the temporal evolution of the phase lag relation between both central neurons. We use different colors to identify the final point using different initial conditions and their relation with the evolution in the other two pictures. Therefore, the color of a point in the left picture is determined (according to the color code represented in the square of colors of plot (B)) by the final position of its transition. For the other two pictures, the color of a point corresponds with the color of delays represented in left picture. (D): Six neurons voltage corresponding to the gait pattern marked by the star, square and circle, respectively, in the three pictures of plot (C). (E): Hexagram corresponding with the same gait pattern. Black rectangles mark time and duration of activation period for each neuron. All the initial conditions taken for this figure belong to the subset  $d_{52} = 0.8$ , with  $d_{12} = d_{45}$  and  $d_{32} = d_{65}$ .

210 color code of the polygonal lines is shown in Figure 9(B) corresponding to the color of the point where  
 211 each simulated curve ends. But this corresponds to the analysis of just 3-cells of the network (CPG),  
 212 and therefore, in order to study the rest of cells, we add two extra plots. The right plot of Figure 9(C)  
 213 takes the same approach as the one on the left, computing the 2D return map showing time evolutions  
 214 of phase lags of the neurons 4 and 6 with respect to the neuron 5 (right side middle-leg). Now we use the  
 215 same initial phase lags and the same color representation as provided by the analysis of the left side (that  
 216 is, we have just the freedom to choose a 2D set of initial conditions, the rest is determined by this set).  
 217 This complementary study provides us the evolution of the right side of the network. Finally, we just  
 218 need to connect both sides, and this is done in Figure 9(C) on the middle plot, showing the evolution of  
 219 the phase lag between the two middle neurons (note that all the delays have been computed with respect  
 220 to the middle neurons). That is, the set of three plots provides us with the complete study of all the  
 221 possible situations for the 2D set of initial conditions used in the phase lag plot on the left.

222 An adequate selection of initial phase lags (for the complete CPG) let us generate the desired 2D  
 223 return map showing time evolutions of phase lags transitioning towards stable fixed points corresponding  
 224 to phase-locked rhythms produced by the subset under consideration. In all the examples of lateral phase  
 225 lag analysis shown in this paper the initial conditions consider a fixed value of  $d_{52}$ , with the symmetry  
 226 conditions  $d_{12} = d_{45}$  and  $d_{32} = d_{65}$  (therefore our free variables are  $d_{12}$  and  $d_{32}$ ), but note that these  
 227 particular restrictions are not a requirement of this technique.

228 Summarizing, we display two planes of phase differences, one for each side, and we connect both sides  
 229 through a representation of the phase difference over time between the two central neurons. In this way,  
 230 we can compute the lag of any neuron with respect to any other. So, we can represent any phase lags  
 231 pattern by combining the three pictures. Remember that these plots are not continuous functions but  
 232 discrete points joined by segments (in Figure 8 the representation was simply the continuous phase space  
 233 evolution), and therefore if the convergence is fast the picture can be quite sharp. In Figure 9 we show an  
 234 example of this lateral phase lag analysis (with initial central delay  $d_{52} = 0.8$ ), together with the signal  
 235 of the pattern corresponding to one of the “equilibrium points” detected, in particular the pattern on the  
 236 dark blue region. In addition to this pattern, at least two extra stable patterns appear, located on the  
 237 green and purple regions. The green pattern is analogous to the blue one, but exchanging the front and  
 238 rear legs of each side. In the purple pattern, located on the diagonal of both side panels, front and rear  
 239 legs move simultaneously. It can be seen that the three patterns have the same lag between the central  
 240 legs. Note that there are also a few lines in light blue color, which correspond to points that remain  
 241 long time in the surroundings of a saddle pattern and therefore it takes a longer integration time of the  
 242 network to converge to the corresponding stable pattern. In any case, the insect will be moving for a  
 243 significant time following the pattern represented by the light blue point.

244 The bottom plots of Figure 9 give two representations of the voltage waveforms. In plot (D) the  
 245 brackets define subsets of the six neurons voltages corresponding to the gait pattern marked by the star,  
 246 square and circle, respectively, in the three pictures of plot (C). And plot (E) shows the “hexagram”  
 247 corresponding with the same gait pattern. Black rectangles mark time and duration of activation period  
 248 for each neuron.

249 The power of the lateral phase lag analysis is that it allows to detect stable, saddle and repulsor  
 250 patterns in a similar way as in [4, 5, 48], and therefore it will help to locate some bifurcations of the  
 251 system [38, 48] and other situations like quasi-periodic lag jitter [48] or other oscillatory behaviors (shown  
 252 as limit cycles in the 2D maps instead of fixed-points that correspond to periodic patterns).

253 We have several remarks on the methodology, first one is that it provides a complete study for the  
 254 selected 2D set of initial conditions, and at this point we have a large freedom, as we have a high  
 255 dimensional differential system (in our case we use as initial conditions the delays on the voltages of the  
 256 neurons 1 and 3 with respect to the neuron 2). Therefore, it gives an analysis of part of all the possible  
 257 situations of the network. On the second hand, and summarizing, for each block of three neurons, we

258 performed Poincaré return maps for phase lags between the central neuron (taken as reference neuron)  
259 and the other two neurons. This methodology can be easily extended to larger networks by performing  
260 the same approach to small groups of 3 neurons using in each set one reference neuron, and studying  
261 also the delays among the control reference neurons. Obviously, if the number of neurons grows, the  
262 approach is more and more cumbersome, but for small CPGs it can provide with some interesting studies  
263 of the dominant patterns. Note that the case of 4-neuron models has been studied in [7] giving a 3D  
264 return map. Finally, although in this paper we have focused on a bursting model, the methodology can  
265 be applied to just active-inactive excitable models like the FitzHugh-Nagumo model (as in [4]) because  
266 we only have to select the voltage value for the Poincaré maps.

#### 267 4.2. Test examples in the insect movement CPG

268 Once the technique is fine-tuned, we can use it to analyze what happens with different values of the  
269 parameters (the integration time for all the figures in this section is 10,000 ms and the initial central  
270 phase lag is 0.8, unless other value is indicated). In Figure 10 we show the lateral phase lag analysis  
271 for different values of  $v_{KS}^{th}$  within the line  $I_{ext} = 35.5$ , analyzed for the isolated neuron in Section 2. In  
272 this figure it can be seen how, as the value of  $v_{KS}^{th}$  increases, the three dominant patterns approach each  
273 other until they end up coinciding and forming the tripod gait. Apart from these dominant patterns, on  
274 this representation we can see patterns with a low number of attracting lines and also more regions with  
275 saddle or repulsor patterns.

276 In the pictures, as the value of the synaptic strength of the network  $g_{syn} = 0.015$  is not too small,  
277 the convergence speed is high, and therefore, the trajectories are abrupt because sometimes in just two  
278 or three steps they reach the attracting point. On the other hand, there are some initial conditions for  
279 which the phase lag between the central neurons ends far from the initial value. Finally, note that the  
280 three dominant patterns follow the same subpattern on both sides of the network because the colors on  
281 the right picture are located in similar positions as on the left one. However, some lines on the right  
282 picture have a color that does not correspond to their position on the left one. Those lines are ending in  
283 points that represent a pattern in which the left side of the network follows a different movement than  
284 the one on the right side (and the color is assigned from the left side as commented in Figure 9). We will  
285 see more clearly some of those patterns in the next section as they are non-symmetric gaits.

286 One of the advantages of this graphical representation of the lateral phase lag patterns is that it is  
287 also possible to visualize which patterns generate overlapping of active periods (see [32] for a detailed  
288 study on the iPRC reduced model) on the same side of the network. Figure 11 shows, for two different  
289 values of  $v_{KS}^{th}$ , the overlapping regions of the neurons 1 and 3 (red lines) and of neuron 1 (or 3) with the  
290 neuron 2 (blue lines). We plot some dashed lines for different values of  $v_{KS}^{th}$  in order to show how the  
291 overlapping area grows as the parameter does, due to the increment of the duty cycle of the neurons, also  
292 related with the number of spikes of the neurons. For instance, in both pictures the pattern in purple  
293 has an overlapping among the extreme neurons on the same side (since the lag of both with the central  
294 neuron is the same). In contrast, the other two dominant patterns do not show any overlapping (between  
295 neurons on the same side), although in the case of  $v_{KS}^{th} = -26$  they are closer to the region of overlapping  
296 between neurons 1 and 3. Taking into account that the duty cycle increases and the three equilibrium  
297 points approach the center of the square as the value of  $v_{KS}^{th}$  increases, there will be a value of  $v_{KS}^{th}$   
298 from which the three dominant patterns will show overlapping between neurons on the same side.

299 Figure 10 was obtained for an integration time of 10,000ms. One remaining question is to analyze if  
300 some observed phenomena are due to some transient dynamics. Figure 12 shows the analysis of the phase  
301 lags on the left side for  $I_{ext} = 35.5$  and  $v_{KS}^{th} = -28$  using two integration times: 10,000ms and 100,000ms.  
302 From the pictures, it is evident that the light blue region is originated from a saddle point that generates  
303 a long transient dynamics region. In any case, note that this transient dynamics may have interest from  
304 the biological point of view as its time duration can be significant, and so that dynamics can be observed

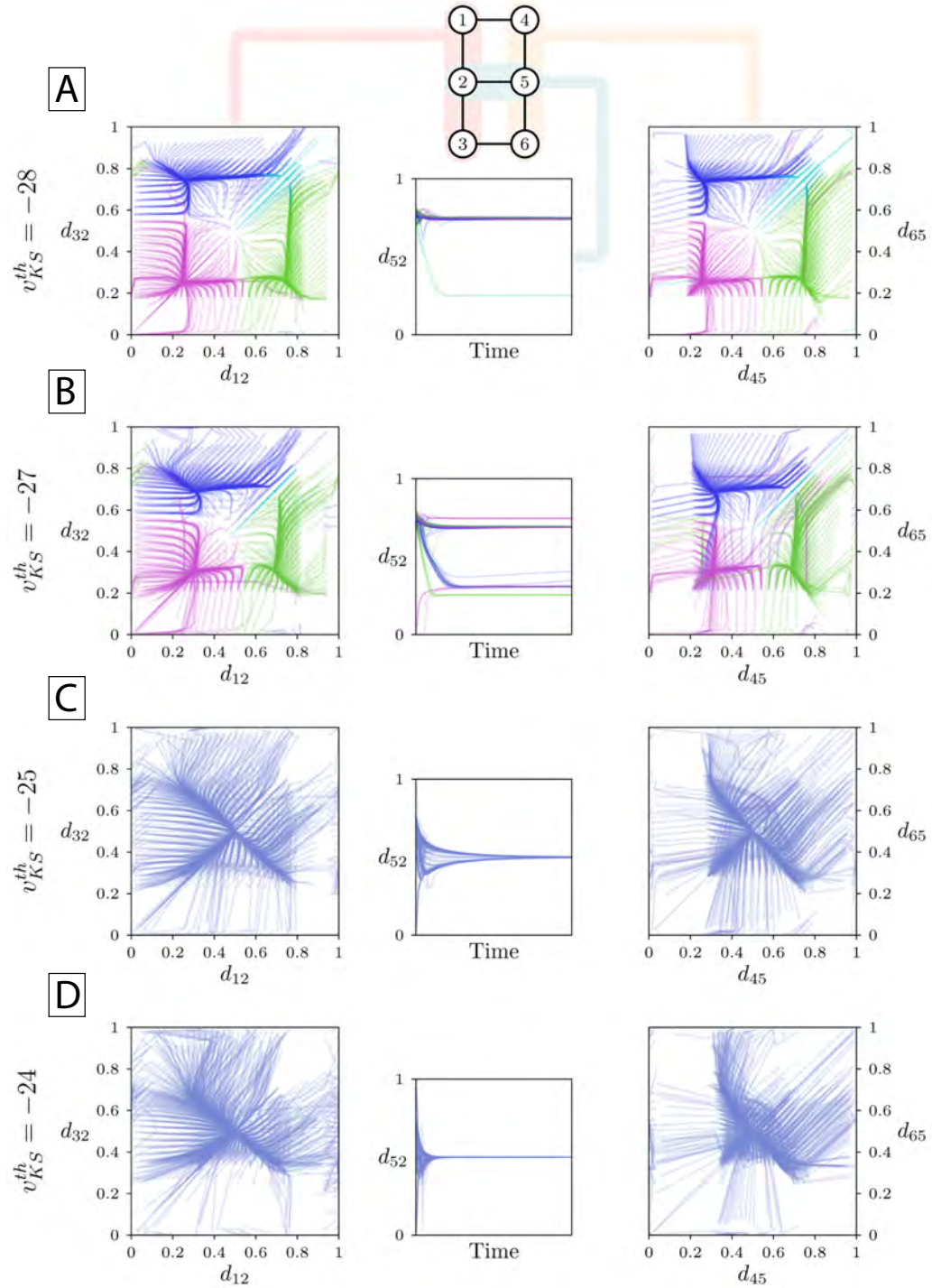


Figure 10: Lateral phase lag analysis for  $I_{ext} = 35.5$ , initial central phase lag 0.8 and different values of  $v_{KS}^{th}$ .

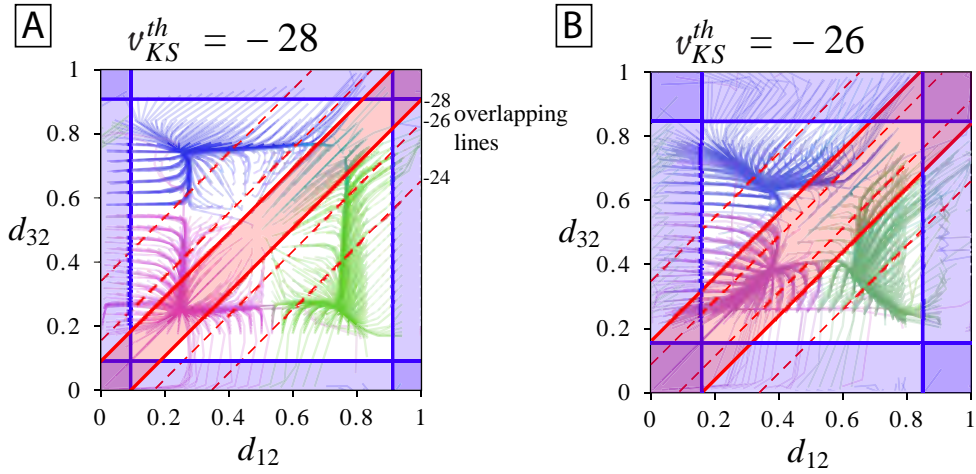


Figure 11: Overlapping areas for the lateral phase lag analysis for  $I_{ext} = 35.5$ , and  $v_{KS}^{th} = -28$  and  $-26$ , that correspond to duty cycle 0.09 and 0.15 of the isolated neuron, respectively. Continuous lines are the overlapping lines for the corresponding value of  $v_{KS}^{th}$ , red color for overlapping between legs 1-3 (both ends), blue color for overlapping between leg 1 or 3 with leg 2 (central).

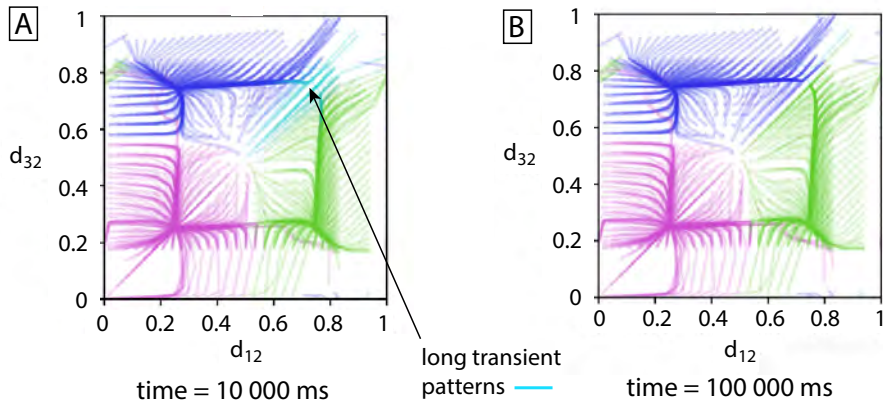


Figure 12: Phase lags on the left side for  $I_{ext} = 35.5$  and  $v_{KS}^{th} = -28$  using two integration times: 10,000ms and 100,000ms.

305 in real systems. The use of two different final times permits to detect some of the transient phenomena  
 306 in the lateral phase lag analysis.

307 The delay between the central neurons is crucial in some patterns. Figure 13 shows the lags between  
 308 the central neurons starting from different initial central phase lags for the two integration times (10,000ms  
 309 and 100,000ms) of Figure 12. The use of a larger integration time permits to eliminate some transient  
 310 dynamics, and so we see more clearly the attracting central patterns. In cases with  $v_{KS}^{th} = -28$  and  $-27$ ,  
 311 we observe a large number of initial conditions with different final central lag. We see that for  $v_{KS}^{th} = -28$   
 312 and  $-27$  the value of central phase lag equal to 0.5 is not part of any stable pattern. This is most clearly  
 313 seen in the longest time integration interval. On the other hand, for  $v_{KS}^{th} = -25$ , that value of central  
 314 delay, 0.5, is the most common one and for  $v_{KS}^{th} = -24$  it is the only attractor that appears. Note that  
 315 the value 0.5 of the central delay is the one of the perfect tripod gait.

316 Another conclusion that can be drawn from Figure 13 is that, depending on the initial values (in

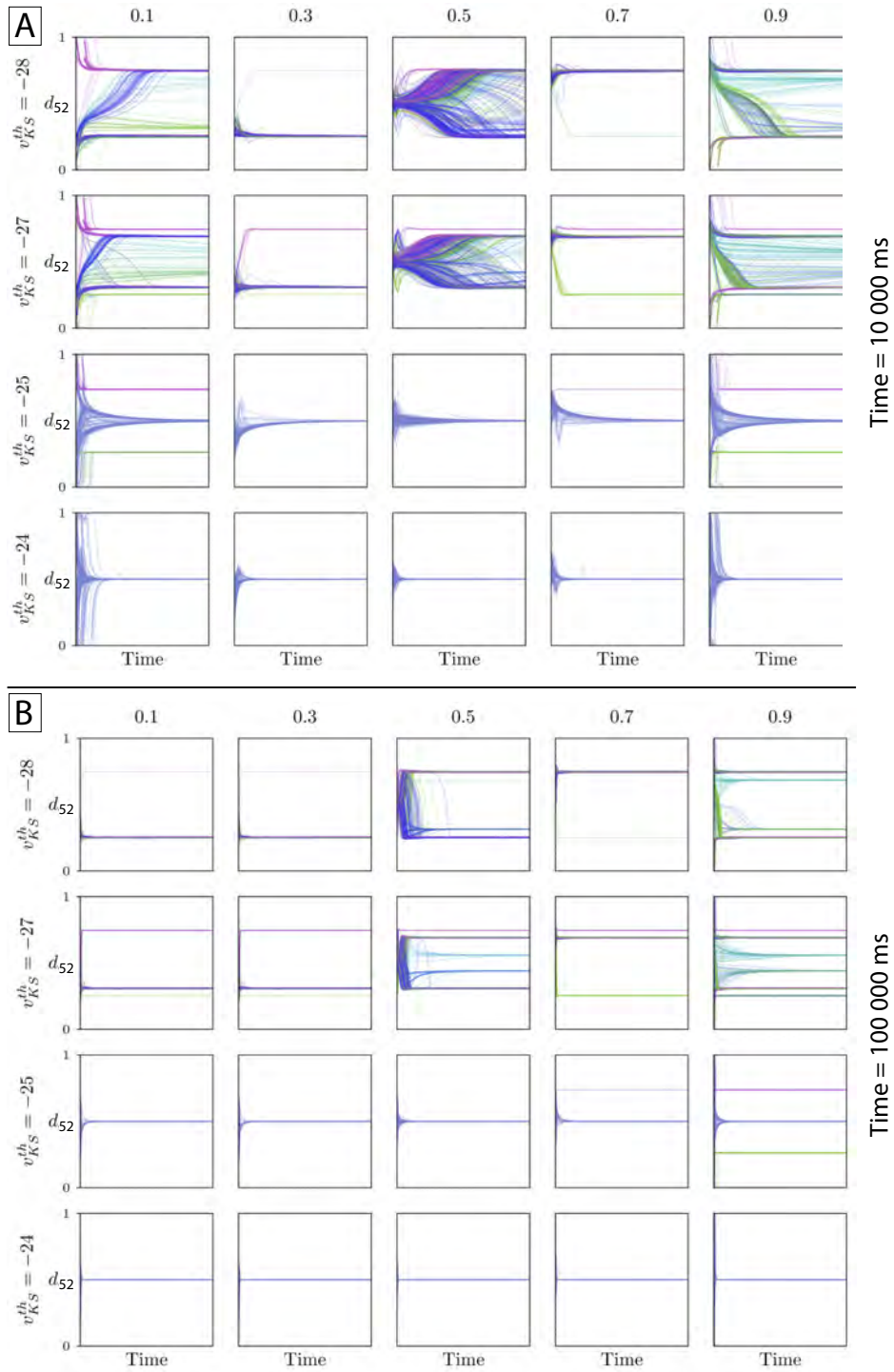


Figure 13: Temporal evolution of phase lag between central neurons  $d_{52}$  using two integration times (10,000ms and 100,000ms) with  $I_{ext} = 35.5$ , different values of  $v_{KS}^{th}$  and initial central phase lags 0.1, 0.3, 0.5, 0.7 and 0.9.

our case, the lag between the central neurons), the stable patterns that are detected may be different. In addition, we are considering initial symmetries that can prevent us from detecting non-symmetric patterns if these symmetries are not broken in the temporal evolution. These facts are limitations of this technique, since, although we work with the complete model of dimension 24, we must restrict ourselves to a 2-dimensional set of initial conditions in order to get an adequate plane representation. And, although we can select any set of dimension two as initial conditions, the possible combinations are so high that they make it impossible to encompass all of them. That is why, in the next section, we will develop a different, less graphic, but more general technique that takes into account the complete space of possible initial conditions.

## 5. Quasi-Monte Carlo pattern sweeping: complete model analysis

The previous section has introduced a two-side analysis of the complete insect movement CPG model. In this section we develop a numerical technique to deal with the complete model without any restriction on the initial conditions.

### 5.1. Numerical method: quasi-Monte Carlo pattern sweeping

In order to detect all kind of patterns, we develop a strategy (*quasi-Monte Carlo pattern sweeping method*) that does not consider any reduction to the system. Therefore, we have to do a large number of simulations for each parametric value and to develop methodologies to classify the different patterns in an automatic way considering 24 dimensional sets of initial conditions.

For a given set of initial conditions, if we observe the variable corresponding to voltage of each neuron, we can appreciate that in most cases their bursts tend to synchronize to a certain *pattern*, that is, a periodic orbit. To identify this pattern, we need to determine the *status* of the network at any instant, that is, which neurons are active (bursting) and which ones are inactive (quiet). Once we have established the *state* for the six neurons, we define the status of the network at any instant with all the states of each neuron. We use an integer number, and in particular its binary representation, in order to reduce at minimum the memory size to store the status of the network at a given instant. Since we are dealing with a six neuron network, a six bit integer suffices to represent its status, assigning each neuron with each position bit, and setting it to 0 when the neuron is relaxed and 1 when it is bursting, that is, the  $i$ -th status  $s_i$  is given by:

$$s_i = \sum_{k=1}^6 \alpha_k 2^{k-1}, \quad \alpha_k = \begin{cases} 1 & \text{if neuron } k \text{ is active} \\ 0 & \text{otherwise} \end{cases}$$

For example, the number 21 (010101 in binary) indicates that neurons 1, 3 and 5 are active. If this status  $s_i$  is different from the one  $s_{i-1}$  on previous integration step, we can infer that at least one neuron has changed its behavior. In that case, we store the previous status  $s_{i-1}$  and the time it has lasted  $t_{i-1}$  into two output vectors to be analyzed in a post-processing stage. Each integration outputs a sequence of integer numbers representing the status of the neuron using the previous scheme, and a sequence of times at which those status are achieved.

As illustration, Figure 14 shows three different patterns, each represented by a sequence of status. The red lines show the limits of the different status. For example, in plot (A) the sequence of status is given by

$$P^1 = \{s_1^1, \dots, s_{10}^1\} = \{1, 0, 32, 0, 4, 20, 16, 0, 10, 0\}.$$

The other two patterns are represented by the sequences of status

$$P^2 = \{s_1^2, \dots, s_{10}^2\} = \{1, 33, 32, 0, 4, 20, 16, 0, 10, 0\},$$

$$P^3 = \{s_1^3, \dots, s_8^3\} = \{33, 0, 4, 20, 16, 0, 10, 0\}.$$

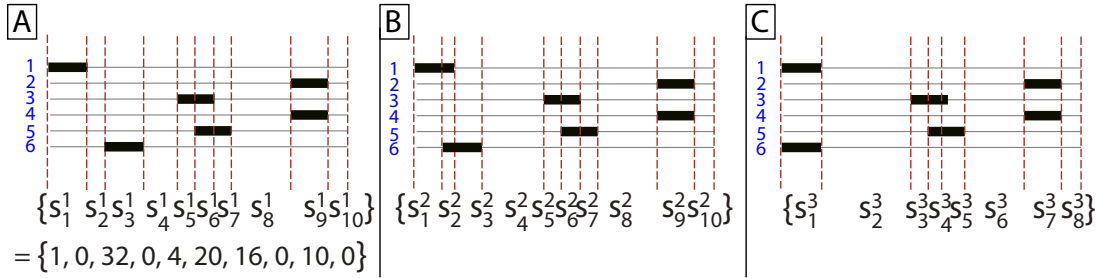


Figure 14: Illustration of the description of three patterns using a finite sequence of status representing the active states among different legs using binary representation (see text for details). The number of status of each sequence is determined by the different active configurations of the pattern shown with the different intervals of time limited by vertical red lines.

Note that the length of each sequence can be different due to the different overlapping situations. This representation, apart from being quite natural, provides us with a formulation quite useful for comparisons among the different patterns (something extremely important if we perform a large number of simulations and we want to have an automatic tool to study all the different patterns).

We remark that in the integration time of the network we have to begin the analysis once the system has converged to a pattern (a limit cycle of the system) or in the negative case to mark as non-convergent (due to a very slow convergence or chaotic behavior). After a transient time of  $10^6$ ms (long enough for our network as our preliminary tests reveal), we start computing the pattern produced by the network. Note that for other networks or systems this transient time has to be set previously in a preliminary analysis of the corresponding problem. When the integration for a particular set of initial conditions is finished, we have output two lists (status and time lapses) that represent the complete *signal* the network is producing. However, the network may generate other kind of signals starting from other initial conditions. Since we are dealing with a 24 dimension differential system, it is infeasible to perform a systematic sweep among all dimensions. Therefore a Monte Carlo approach is the only reasonable one. Instead of using classical pseudorandom number generation (like the Mersenne Twister), we sacrifice the entropy of the numbers in favor to low discrepancy (they can be used as pseudorandom for many purposes). Hence, we use 24-dimensional Halton sequences [49], that cover a hypercube uniformly, to generate up to  $M$  (in our case  $M = 200$ ) initial conditions of the network for a fixed set of parameters. In case of being interested in a much more detailed analysis of a particular set of parameters, the number of initial conditions  $M$  can be raised in order to locate pattern gaits with a small basin of attraction. In this process we have also taken into account the range of each variable in order to consider the complete space where the model evolves. For a neuron in our particular model, the initial condition of its first variable is chosen to be in  $[-40, 10]$  that covers all the possible values (when decoupled), since it represents a voltage. For the other variables the initial value is set in the interval  $[0, 1]$  as they are gating variables.

Now, after one Monte Carlo simulation for a fixed set of parameters, we have  $M = 200$  simulations of the network. Once the status sequence for each one is obtained, the next task is to extract the periodic pattern (if any) from each simulation and keep it in a final list, if it is different from those in the list. So, we have to determine if two patterns are the same or symmetric ones. This is a post-processing stage, where we analyze each sequence.

In more detail, the extraction of periodic patterns from a sequence is done as follows:

- (1) Delete from both output lists all *status* that last less than  $t_{small}$  in order to consider only significant changes (in our case we consider  $t_{small} = 0.03$ ms). The vector of time lapses is used in this stage.
- (2) Compute an auxiliary list containing the logarithm of the 6-bit status signals, so that we have small enough numbers. Small numbers perform better in Fast Fourier Transforms, since they are more balanced, and the magnitude of the numbers is meaningless in all this process.

- 390 (3) Compute the Fast Fourier Transform of the auxiliary logarithm list, and search for the best guess  
391 of the period (or quasi period) of the *signal*, read as number of *status* the *signal* is made of. We  
392 remark that we are counting the number of *status* for each period, not the time lapses (which are  
393 provided by the intervals of time list). For instance, in Figure 14(A) the pattern has a period of 10  
394 *status*.
- 395 (4) Prune both the *signal* and time lapse lists to the last period, and compare it with all previous  
396 *patterns* to detect if it is the same *pattern* with a time shift (a rotational symmetry) or a symmetry  
397 of the network (left-right or front-back side of an insect in our case). That is, we check if it belongs  
398 to the same *equivalence class* as some previous *pattern*.
- 399 (5) If a new *equivalence class* is found, it is added to the list of *equivalence classes* using a representative  
400 of it. In the opposite case, the corresponding *equivalence class* counter is incremented by one (this  
401 counter will give us the percentage of each *equivalence class* for a selected parameter).

402 After this pruning, we have the dominant patterns for that network at fixed parameter values. Expe-  
403 rience has shown us that in a system there are some dominant patterns, and marginal ones with a small  
404 basin of attraction. Note that, for this reason, depending on the number of initial conditions in the quasi-  
405 Monte Carlo method, some of the marginal patterns may not be detected, but the most representative  
406 ones are always obtained.

407 Up to this point, we have studied in detail the network for a particular value of its parameters. Now  
408 we finally can make a sweep varying uniformly the value of one parameter to observe the transition from  
409 one dominant pattern to another. Note that the different patterns evolve when a parameter changes. For  
410 instance, in Figure 14 we show some of the observed evolutions. In this case we illustrate changes on the  
411 neurons 1 and 6, and how the overlapping of their active states evolve from no overlapping to perfect  
412 synchronization (we allow small discrepancies). All these situations (and much more options taking into  
413 account that we have 6 neurons) can be detected with the proposed algorithm. To describe the parametric  
414 evolution we have to add a new extra final step to the algorithm after each parametric value has been  
415 analyzed and obtained a set of equivalence classes of the different patterns:

416 Compare all the *equivalence classes* for the current value of parameters with the previously generated  
417 list with the former analyzed values of parameters. If a new *equivalence class* is found, it is added  
418 to the list of *equivalence classes* using a representative of its *equivalence class*.

419 As a result we have a list with all the patterns found (equivalence classes) and, for each value of  
420 parameters, the percentage of its appearance.

421 Due to the generic approach of this methodology, it can be applied to any small network, simply  
422 adapting the binary approach to the total number of neurons of the network. Obviously, increasing the  
423 dimension will also require an increase in the number of initial conditions to obtain a complete analysis.

## 424 5.2. Test examples in the insect movement CPG

425 In Figure 15 we show a summary of the results obtained by applying the technique described above  
426 (quasi-Monte Carlo pattern sweeping) in the bursting interval  $v_{KS}^{th} \in [-29.67, -22.54]$ , with  $I_{ext} =$   
427 35.5, on the selected line indicated in Figure 5. The central panel summarizes the final result of the  
428 above numerical approach, a list with all the patterns found (equivalence classes) and, for each value of  
429 parameters, the percentage of their appearance. Note that each different color represents a particular  
430 equivalence class of patterns and some label numbers will show different patterns of the same class in  
431 order to illustrate the evolution inside each equivalence class. The sum of all the percentages shown at  
432 many points does not reach 100% because only those patterns with a minimum percentage of 5% in some  
433 value of the line are represented. We can see how the distance to 100% is greater at some points where  
434 a spike-adding process occurs for isolated neuron analysis (see the small band with the spike-counting  
435 technique showing the number of spikes of the attracting bursting periodic orbit for the isolated neuron).

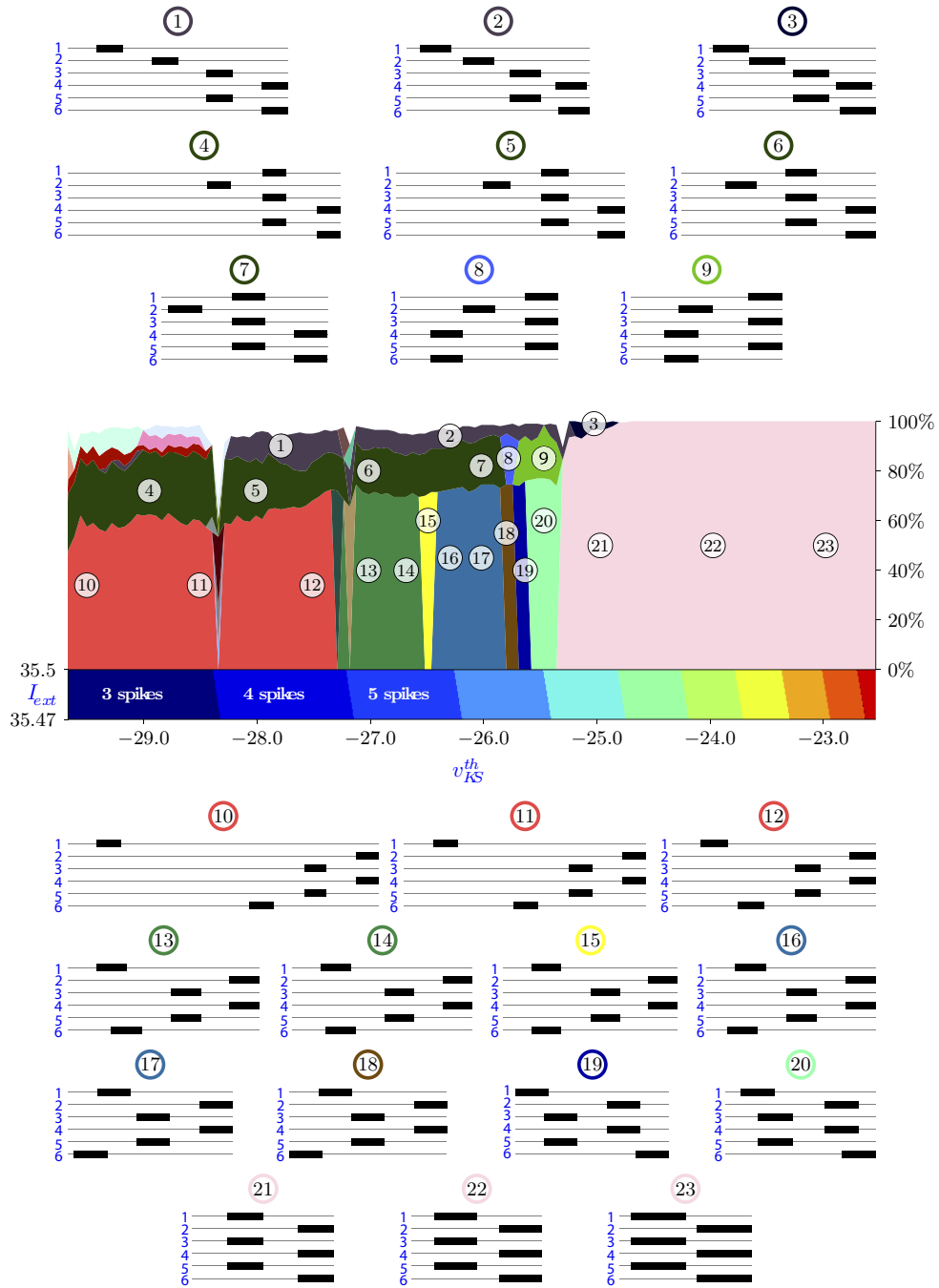


Figure 15: Complete pattern radiography using the quasi-Monte Carlo pattern sweeping on the horizontal line  $I_{ext} = 35.5$ . The central panel shows the percentage of initial conditions that converge to a certain pattern. Each color identifies a equivalence class of patterns (see the text for more details). A thin spike-counting band is also shown indicating the number of spikes of the attractor orbit for an isolated neuron. At the top and bottom, some hexagrams corresponding to the main movement patterns are shown.

436 The reason for these “valleys” is that the isolated neuron undergoes a process of change in which two  
 437 orbits with a different number of spikes coexist. This circumstance originates a large number of patterns  
 438 with very little significance and low stability that are not represented in the figure. In fact, most of these  
 439 patterns are unstable (saddles) but, during a long enough transient, the dynamics of the network starting  
 440 at some initial conditions remains close to them.

441 On the top and bottom part of the figure we plot the most representative hexagrams. In the lower  
 442 part of the figure we represent the hexagrams of the dominant pattern. The length of the hexagrams  
 443 is proportional to the period of the pattern (periodic orbit) in order to also observe the changes in the  
 444 period. If we move from pattern number  $-10-$  to  $-15-$ , we can see how the period decreases as  $v_{KS}^{th}$   
 445 increases. This causes the active intervals of neurons 1 and 6 to approach, so that in pattern  $-13-$  they  
 446 partially overlap (hence the color difference in the central panel), to synchronize exactly later in the  
 447 pattern  $-15-$ , giving the perfect *tetrapod gait*. The relative displacement of the active intervals of neurons  
 448 1 and 6 continues, so that neuron 1 starts to overtake neuron 6 beginning to overlap with the active  
 449 intervals of neurons 3 and 5 that are simultaneous in all the dominant patterns. On the other hand, the  
 450 active interval of the neuron 6 does the same with the simultaneous neurons 2 and 4. Both overlays are  
 451 increasing (due to the increased duty cycle, see Figure 11) until, in pattern  $-21-$ , the active intervals  
 452 of neurons 1, 3 and 5 on one hand and 2, 4 and 6 on the other, are simultaneous, reaching the perfect  
 453 *tripod gait*. Note that along this paper we assimilate into the same equivalence class, due to the chosen  
 454 symmetric coupling coefficients  $c_i$ , two different patterns where one of them is the result of applying to  
 455 the other a reflection of left-right and/or forward-backward. So, the patterns represented in blue and  
 456 green areas in Figure 10 belong to the same equivalence class than the patterns from  $-10-$  to  $-20-$ .

457 In the upper part of Figure 15, we show the evolution of non-dominant patterns, but with a significant  
 458 percentage of initial conditions converging to these patterns. The second most represented pattern  
 459 corresponds to the purple pattern of Figure 10 and it evolves, in Figure 15, along the patterns from  
 460  $-4-$  to  $-9-$ . If we observe these patterns, we can see that from patterns  $-4-$  to  $-7-$  there is a decrease  
 461 in the period as the value of  $v_{KS}^{th}$  increases. This reduction of the period originates that, in pattern  $-8-$ ,  
 462 the active intervals of neurons 4 and 6 (which are simultaneous) begin to overlap with that of neuron 2  
 463 until, finally, the perfect tripod gait is reached. This situation is similar to that previously described for  
 464 the dominant pattern. In addition, we can see that the absorption of the three patterns by the tripod  
 465 gait is detected simultaneously due to the symmetry in the coefficients  $c_i$ .

466 Finally, we discuss the evolution of the patterns from  $-1-$  to  $-3-$ . These patterns are very difficult  
 467 to detect with the technique used in the previous Section 4 since, as  $d_{12} \neq d_{45}$ , they do not fulfil one of  
 468 the restrictions imposed on the subset from which we took the initial conditions. These patterns may  
 469 correspond to some of the “dislodged” color points observed in Figure 10, which represent a different kind  
 470 of movement of the insect’s legs on one side and on the other. As in the previous cases, a reduction of  
 471 the period is observed. The difference is that this pattern does not seem to converge to the tripod gait,  
 472 but its basin of attraction decreases until it disappears.

473 Therefore, Figure 15 explains the process by which the tripod becomes the only dominant pattern,  
 474 either by convergence or disappearance of certain patterns.

475 Note that the studied line crosses several spike-adding bands on the selected interval, and so we see  
 476 how on these changes there are more strange (or slightly different) patterns due, in some circumstances,  
 477 to very long transients. This is clearly seen, for instance, in the change from three to four spikes on  
 478 the corresponding isolated neuron, where a lot of thin strips of pattern colors are present. From other  
 479 numerical tests, it seems that the changes along the entire bursting region will be quite similar in all  
 480 the parametric phase space and the differences will be mainly on low percentage patterns, being some of  
 481 them quite strange.

482 Although analyzing non-dominant patterns is beyond the scope of this paper, and just to show how  
 483 some odd patterns are present, we show in Figure 16 the time signal of the five dominant stable patterns

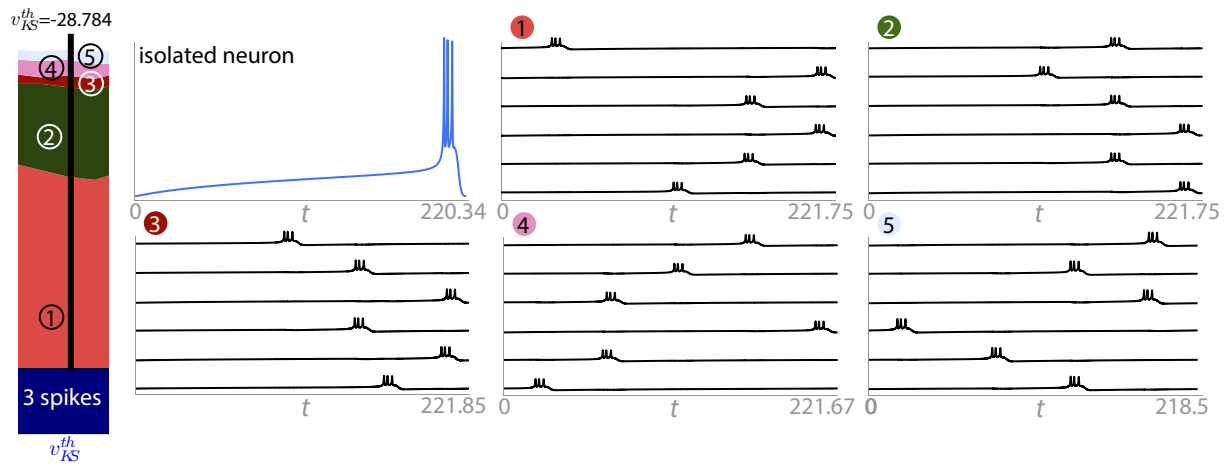


Figure 16: Time signal of different patterns for  $I_{ext} = 35.5$  and  $v_{KS}^{th} = -28.784$ . The color circle identifies each signal with the pattern marked in Figure 15 (see also the color band on the left side).

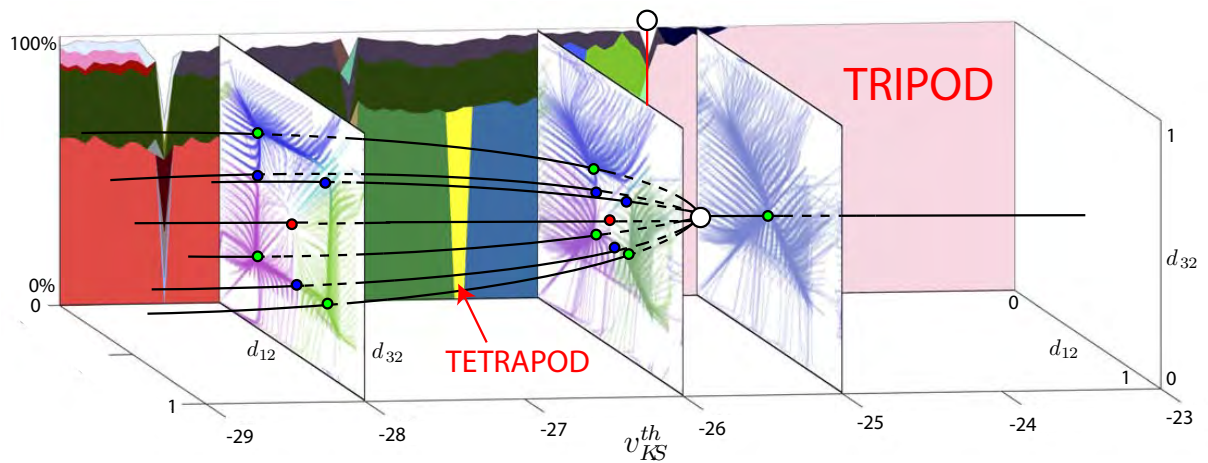


Figure 17: Graphic combination of sweeping techniques described in Sections 4 (lateral phase lag analysis) and 5 (quasi-Monte Carlo pattern sweeping). Green points represent sinks (attractors); blue points represent saddle points and red points sources (repulsors).

484 detected for the value of the parameters:  $I_{ext} = 35.5$  and  $v_{KS}^{th} = -28.784$ . The color of the circle that  
485 accompanies each signal is the same as the color that identifies the different patterns in the central panel  
486 of Figure 15. On the left side we have extracted a color band from that central panel in order to locate  
487 the different patterns. The first two points correspond to the dominant patterns (also perfectly detected  
488 with the technique of lateral convergence). As previously mentioned, these patterns present the same  
489 movement in the legs of each side, simply with a lag between both sides. On the other hand, the other  
490 three patterns show a clear asymmetry between the movement of left and right legs. Note that these  
491 patterns cannot be detected with the methods that use several symmetry reductions. We also represent  
492 the periodic orbit of the model of an isolated neuron to show how, individually, each neuron within the  
493 network has a similar dynamical behavior to the one of the isolated neuron, both in the number of spikes  
494 and in the period of the orbit. In fact, in general, all patterns detected for a fixed set of parameters have  
495 a very similar duration, with maximum differences of less than 5% in most cases. Exceptions to this  
496 situation are some patterns that need two periods of activation of each neuron to close the orbit, and in  
497 the area near the appearance of the perfect tripod gait where differences close to 20% in the period can  
498 be reached.

499 Finally, we note that Figure 15 explains in more detail than Figure 10 the evolution of the dominant  
500 patterns until they end up converging to the tripod gait. However, Figure 10 shows the stable and unstable  
501 equilibria of the phase lag maps of the model and its evolution by modifying the control parameter. In  
502 order to summarize all the results, in Figure 17 we combine both figures to show how in addition to  
503 the three stable equilibria of the return map, corresponding to the three dominant patterns, there are at  
504 least four other unstable equilibria (note that other points may be present). All these points seem to end  
505 up converging to the tripod gait in a very degenerate bifurcation where all the points apparently collide  
506 into the stable tripod gait point. This situation is analogous to that observed in [34, case  $\alpha = 1/2$ ] with  
507 the reduced 2D iPRC model for the symmetric case and using `Matcont` bifurcation software. In our case  
508 we detect that bifurcation for the complete model and without using any continuation software, just by  
509 computing a sweep (as in [48]) of the interval studied using the techniques described above. Also, it is  
510 important to remark that the mixture of techniques permits us to detect in a mathematical model most  
511 of the experimental patterns illustrated in classical references [37, 50].

## 512 Conclusions

513 In this paper we have adapted different numerical techniques and we have combined them to develop  
514 new tools to analyze small networks. As an important test problem, we have studied in some detail  
515 the particular case of the complete six neurons model of the CPG that controls the movement of some  
516 insects. As first step, we show how the previous study of the model of an isolated neuron provides us  
517 with valuable information to determine the parametric region of interest and some dynamical system  
518 information.

519 Once we have obtained the “roadmap” that gives us the analysis of an isolated neuron, we have  
520 designed a tool (lateral phase lag analysis) that visualizes the evolution of the delay of one neuron with  
521 respect to the rest of the network. This tool is based on the analysis of the lateral phase lags on both sides  
522 of the network, complemented with the study of the delay of the two central neurons. This technique  
523 (an extension of the technique introduced in [51] for 3-cell CPGs) gives us information similar to that  
524 obtained in [34] for the reduced model of oscillators, but in our case working with the complete model  
525 of neurons. With this tool we can study the evolution of the dominant patterns and the equilibrium  
526 points that generate them. However, since we work with planar representations, for the result to be  
527 significant, we have to restrict the set of initial conditions to a space of dimension two. Since the model  
528 has dimension 24, the described limitation causes that we may miss patterns whose basin of attraction  
529 has empty intersection with the selected subset of initial conditions. Using a proper selection of groups  
530 of three neurons, this methodology can be used in different models than the CPG studied in this paper.

531 We have developed another algorithm (quasi-Monte Carlo pattern sweeping) to eliminate the limi-  
532 tations of the former technique. Now we use initial conditions covering the space of dimension 24 that  
533 controls the complete model of the network. This methodology allows to study the different patterns of  
534 the model and automatically classifies these patterns. With this algorithm we are able to perform a sweep  
535 leaving one of the system parameters free to study the changes produced. The sweep results permit us to  
536 understand much better how dominant patterns are evolving until they end up converging to the tripod  
537 gait in the case of insect movement. On the other hand, we have located different odd patterns that  
538 are difficult to locate by other means and that have interesting asymmetries. Since this methodology is  
539 based only on a selection of appropriate initial conditions and on an optimal automatic pattern analysis  
540 by using Fourier techniques and a binary representation of each pattern, it can be used in small networks  
541 in general.

542 Besides, we have shown that the mixture of both techniques permits us to detect in a model most  
543 of the experimental patterns presented in classical papers [37], that also gives a hypothesis relating the  
544 various six-legged gaits.

545 The combination of all the numerical techniques described in this paper opens a door to a deeper  
546 understanding of insect movement CPGs. In addition, it also allows to study any small CPG, without  
547 restriction on symmetries or heterogeneity between the neurons of the network that comprise it.

## 548 Acknowledgments

549 RB, MR and SS have been supported by the Spanish Research project PGC2018-096026-B-I00, and  
550 European Regional Development Fund and Diputación General de Aragón (Ref. E24-17R and LMP124-  
551 18). Ál has been supported by the Spanish Research project MTM2016-77642-C2-2-P, and European  
552 Regional Development Fund and Diputación General de Aragón (Ref. E22-17R and). RB, Ál and SS  
553 has been supported by the Universidad de Zaragoza-CUD project UZCUD2019-CIE-04.

- 554 [1] P. Ashwin, Symmetric chaos in systems of three and four forced oscillators, *Nonlinearity* 3 (3) (1990) 603–617.
- 555 [2] P. Ashwin, O. Burylko, Y. Maistrenko, Bifurcation to heteroclinic cycles and sensitivity in three and four coupled  
556 phase oscillators, *Physica D* 237 (4) (2008) 454–466.
- 557 [3] M. Aguiar, P. Ashwin, A. Dias, M. Field, Dynamics of coupled cell networks: Synchrony, heteroclinic cycles and  
558 inflation, *Journal of Nonlinear Science* 21 (2) (2011) 271–323.
- 559 [4] J. T. C. Schwabedal, D. E. Knapper, A. L. Shilnikov, Qualitative and quantitative stability analysis of penta-rhythmic  
560 circuits, *Nonlinearity* 29 (12) (2016) 3647–3676.
- 561 [5] J. Wojcik, J. Schwabedal, R. Clewley, A. L. Shilnikov, Key bifurcations of bursting polyrhythms in 3-cell Central  
562 Pattern Generators, *PLOS ONE* 9 (4) (2014) 1–27.
- 563 [6] M. Lodi, A. Shilnikov, M. Storace, Design of synthetic central pattern generators producing desired quadruped gaits,  
564 *IEEE Transactions on Circuits and Systems I: Regular Papers* 65 (3) (2018) 1028–1039.
- 565 [7] S. Jalil, D. Allen, J. Youker, A. Shilnikov, Toward robust phase-locking in Melibe swim central pattern generator  
566 models, *Chaos* 23 (4) (2013) 046105.
- 567 [8] P. Ashwin, S. Coombes, R. Nicks, Mathematical frameworks for oscillatory network dynamics in neuroscience, *The*  
568 *Journal of Mathematical Neuroscience* 6:2 (2016).
- 569 [9] S. Daun, J. E. Rubin, I. A. Rybak, Control of oscillation periods and phase durations in half-center central pattern  
570 generators: a comparative mechanistic analysis, *Journal of Computational Neuroscience* 27 (1) (2009) 3–36.
- 571 [10] E. Marder, D. Bucher, Central pattern generators and the control of rhythmic movements, *Current Biology* 11 (23)  
572 (2001) R986–R996.
- 573 [11] A. Selverston, *Model Neural Networks and Behavior*, Springer, Berlin, 1985.
- 574 [12] T. Bal, F. Nagy, M. Moulins, The pyloric central pattern generator in crustacea: a set of conditional neural oscillators,  
575 *Journal of Comparative Physiology A* 163 (1996) 715–727.
- 576 [13] E. Marder, R. Calabrese, Principles of rhythmic motor pattern generation, *Physiol Rev* 76 (1996) 687–717.
- 577 [14] W. Kristan, R. L. Calabrese, Rhythmic swimming activity in neurones of the isolated nerve cord of the leech, *The*  
578 *Journal of Experimental Biology* 65 (3) (1976) 643–668.
- 579 [15] M. A. Masino, R. L. Calabrese, Phase relationships between segmentally organized oscillators in the leech heartbeat  
580 pattern generating network, *Journal of Neurophysiology* 87 (3) (2002) 1572–1585.
- 581 [16] M. A. Masino, R. L. Calabrese, Period differences between segmental oscillators produce intersegmental phase differ-  
582 ences in the leech heartbeat timing network, *Journal of Neurophysiology* 87 (3) (2002) 1603–1615.

- 583 [17] R. L. Calabrese, B. J. Norris, A. Wenning, T. M. Wright, Coping with variability in small neuronal networks, *Integrative*  
584 *and Comparative Biology* 51 (6) (2011) 845–855.
- 585 [18] D. G. Lamb, R. L. Calabrese, Neural circuits controlling behavior and autonomic functions in medicinal leeches, *Neural*  
586 *Systems & Circuits* 1 (1) (2011) 1–10.
- 587 [19] A. J. Ijspeert, Central pattern generators for locomotion control in animals and robots: A review, *Neural Networks*  
588 21 (4) (2008) 642–653.
- 589 [20] K. Mombaur, K. E. Berns, *Modeling, Simulation and Optimization of Bipedal Walking*, Springer-Verlag, Berlin Hei-  
590 delberg, 2013.
- 591 [21] A. Ayali, A. Borgmann, A. Büschges, E. Couzin-Fuchs, S. Daun-Gruhn, P. Holmes, The comparative investigation of  
592 the stick insect and cockroach models in the study of insect locomotion, *Current Opinion in Insect Science* 12 (2015)  
593 1–10.
- 594 [22] S. Fujiki, S. Aoi, T. Funato, N. Tomita, K. Senda, K. Tsuchiya, Hysteresis in the metachronal-tripod gait transition  
595 of insects: A modeling study, *Phys. Rev. E* 88 (2013) 012717.
- 596 [23] R. Ritzmann, S. N. Zill, *Neuroethology of Insect Walking*, Scholarpedia 8 (9) (2013) 30879.
- 597 [24] R. Ghigliazza, P. Holmes, A minimal model of a central pattern generator and motoneurons for insect locomotion,  
598 *SIAM Journal on Applied Dynamical Systems* 3 (4) (2004) 671–700.
- 599 [25] T. I. Toth, J. Schmidt, A. Büschges, S. Daun-Gruhn, A neuro-mechanical model of a single leg joint highlighting the  
600 basic physiological role of fast and slow muscle fibres of an insect muscle system, *PLOS ONE* 8 (11) (2013) 1–12.
- 601 [26] C. Mantziaris, T. Bockemühl, P. Holmes, A. Borgmann, S. Daun, A. Büschges, Intra- and intersegmental influences  
602 among central pattern generating networks in the walking system of the stick insect, *Journal of Neurophysiology* 118 (4)  
603 (2017) 2296–2310.
- 604 [27] E. Tytell, P. Holmes, A. Cohen, Spikes alone do not behavior make: why neuroscience needs biomechanics, *Current*  
605 *Opinion in Neurobiology* 21 (5) (2011) 816–822.
- 606 [28] F. Tedeschi, G. Carbone, Design issues for hexapod walking robots, *Robotics* 3 (2) (2014) 181–206.
- 607 [29] J. C. Spagna, D. I. Goldman, P.-C. Lin, D. E. Koditschek, R. J. Full, Distributed mechanical feedback in arthropods  
608 and robots simplifies control of rapid running on challenging terrain, *Bioinspiration & Biomimetics* 2 (1) (2007) 9–18.
- 609 [30] J. J. Collins, I. Stewart, Hexapodal gaits and coupled nonlinear oscillator models, *Biological Cybernetics* 68 (4) (1993)  
610 287–298.
- 611 [31] F. Herrero-Carrón, F. B. Rodríguez, P. Varona, Bio-inspired design strategies for central pattern generator control in  
612 modular robotics, *Bioinspiration & Biomimetics* 6 (1) (2011) 016006.
- 613 [32] A. Yeldesbay, T. Tóth, S. Daun, The role of phase shifts of sensory inputs in walking revealed by means of phase  
614 reduction, *Journal of Computational Neuroscience* 44 (3) (2018) 313–339.
- 615 [33] J. J. Collins, I. N. Stewart, Coupled nonlinear oscillators and the symmetries of animal gaits, *Journal of Nonlinear*  
616 *Science* 3 (1) (1993) 349–392.
- 617 [34] Z. Aminzare, V. Srivastava, P. Holmes, Gait transitions in a phase oscillator model of an insect central pattern  
618 generator, *SIAM Journal on Applied Dynamical Systems* 17 (1) (2018) 626–671.
- 619 [35] B. Ermentrout, Type I membranes, phase resetting curves, and synchrony, *Neural Comput.* 8 (5) (1996) 979–1001.
- 620 [36] M. Schwemmer, T. Lewis, The theory of weakly coupled oscillators, in: *Phase Response Curves in Neuroscience:*  
621 *Theory, Experiment, and Analysis*, Vol. 1151 of *Lecture Notes in Math.*, Springer, New York, 2012, pp. 3–31.
- 622 [37] D. M. Wilson, Insect walking, *Annual Review of Entomology* 11 (1) (1966) 103–122.
- 623 [38] Á. Lozano, M. Rodríguez, R. Barrio, Control strategies of 3-cell central pattern generator via global stimuli, *Scientific*  
624 *Reports* 6 (2016) 23622.
- 625 [39] Z. Aminzare, P. Holmes, Heterogeneous inputs to central pattern generators can shape insect gaits, *SIAM Journal on*  
626 *Applied Dynamical Systems* 18 (2) (2019) 1037–1059.
- 627 [40] E. Doedel, AUTO: a program for the automatic bifurcation analysis of autonomous systems, in: *Proceedings of the*  
628 *Tenth Manitoba Conference on Numerical Mathematics and Computing*, Vol. I (Winnipeg, Man., 1980), Vol. 30, 1981,  
629 pp. 265–284.
- 630 [41] J. Rinzel, A formal classification of bursting mechanisms in excitable systems, in: E. Teramoto, M. Yumaguti (Eds.),  
631 *Mathematical Topics in Population Biology, Morphogenesis and Neurosciences: Proceedings of an International Sym-*  
632 *posium held in Kyoto, November 10–15, 1985*, Springer Berlin Heidelberg, Berlin, Heidelberg, 1987, pp. 267–281.
- 633 [42] E. M. Izhikevich, Neural excitability, spiking and bursting, *International Journal of Bifurcation and Chaos* 10 (06)  
634 (2000) 1171–1266.
- 635 [43] R. Barrio, M. A. Martínez, S. Serrano, A. Shilnikov, Macro- and micro-chaotic structures in the Hindmarsh–Rose  
636 model of bursting neurons, *Chaos* 24 (2) (2014) 023128.
- 637 [44] D. Linaro, A. Champneys, M. Desroches, M. Storace, Codimension-two homoclinic bifurcations underlying spike adding  
638 in the Hindmarsh–Rose burster, *SIAM J. Appl. Dyn. Syst.* 11(3) (2012) 939–962.
- 639 [45] D. Terman, The transition from bursting to continuous spiking in excitable membrane models, *Journal of Nonlinear*  
640 *Science* 2 (2) (1992) 135–182.
- 641 [46] R. Barrio, F. Blesa, S. Serrano, Qualitative analysis of the Rössler equations: Bifurcations of limit cycles and chaotic  
642 attractors, *Physica D: Nonlinear Phenomena* 238 (2009) 1087–1100.
- 643 [47] V. D. Witte, W. Govaerts, Y. Kuznetsov, H. Meijer, Analysis of bifurcations of limit cycles with Lyapunov exponents

- 644 and numerical normal forms, *Physica D: Nonlinear Phenomena* 269 (2014) 126–141.
- 645 [48] R. Barrio, M. Rodríguez, S. Serrano, A. Shilnikov, Mechanism of quasi-periodic lag jitter in bursting rhythms by a  
646 neuronal network, *EPL* 112 (3) (2015) 38002.
- 647 [49] J. H. Halton, On the efficiency of certain quasi-random sequences of points in evaluating multi-dimensional integrals,  
648 *Numerische Mathematik* 2 (1) (1960) 84–90.
- 649 [50] D. Graham, Pattern and control of walking in insects, *Advances in Insect Physiology* 18 (1985) 31–140.
- 650 [51] J. Wojcik, J. Schwabedal, R. Clewley, A. L. Shilnikov, Key bifurcations of bursting polyrhythms in 3-cell central  
651 pattern generators, *PloS One* 9 (4) (2014) e92918.